1   **Revision 3 (MS 8250)**

2   **word count: 11322**

3   **An ab-initio study on the thermodynamics of disulfide, sulfide, and bisulfide**

4   **incorporation into apatite and the development of a more comprehensive temperature,**

5   **pressure, pH, and composition-dependent model for ionic substitution in minerals**

6   **YoungJae Kim[1,2,*], Brian Konecke[1,3], Adam Simon[1], Adrian Fiege[1], Udo Becker[1],**

7   [1]University of Michigan, Department of Earth and Environmental Sciences, Ann Arbor, MI

8   48109, USA

9   [2]Chemical Sciences and Engineering Division, Argonne National Laboratory, Lemont,

10   Illinois 60439, USA

11   [3]Fathom Geophysics, LLC. 12956 Claylick Rd, Neward, Ohio 43056, USA

12   * corresponding author; E-mail: youngjkm@umich.edu

13

Abstract

15   The mineral apatite, $Ca_{10}(PO_4)_6(F,OH,Cl)_2$, incorporates sulfur (S) during crystallization

16   from S-bearing hydrothermal fluids and silicate melts. Our previous studies of natural and

17   experimental apatite demonstrate that the oxidation state of S in apatite varies systematically as a

18   function of oxygen fugacity (fO_2). The S oxidation states -1 and -2 were quantitatively

19   identified in apatite crystallized from reduced, S-bearing hydrothermal fluids and silicate melts

20   by using sulfur K-edge X-ray absorption near-edge structure spectroscopy (S-XANES) where

21    $S^{6+}/\Sigma S$ in apatite increases from ~0 at FMQ−1 to ~1 at FMQ+2, where FMQ refers to the

22   fayalite-magnetite-quartz fO_2 buffer. In this study, we employ quantum-mechanical calculations

23   to investigate the atomistic structure and energetics of S(-I) and S(–II) incorporated into apatite

24   and elucidate incorporation mechanisms.

25   One S(–I) species (disulfide, S_2^{2-}) and two S(–II) species (bisulfide, HS^-, and sulfide, S^{2-})

26   are investigated as possible forms of reduced S species in apatite. In configuration models for the

27   simulation, these reduced S species are positioned along the c-axis channel, originally occupied

28   by the column anions F, Cl, and OH in the endmember apatites. In the lowest-energy

29   configurations of S-incorporated apatite, disulfide prefers to be positioned halfway between the

30   mirror planes at $z = 1/4$ and $3/4$. In contrast, the energy-optimized bisulfide is located slightly

31   away from the mirror planes by ~0.04 fractional units in the c direction. The energetic stability of

32   these reduced S species as a function of position along the c-axis can be explained by the

33   geometric and electrostatic constraints of the Ca and O planes that constitute the c-axis channel.

34   The thermodynamics of incorporation of disulfide and bisulfide into apatite are evaluated by

35   using solid-state reaction equations where the apatite host and a solid S-bearing source phase

36   (pyrite and $Na_2S_{2(s)}$ for disulfide; troilite and $Na_2S_{(s)}$ for sulfide) are the reactants, and the S-

37   incorporated apatite and an anion sink phase are the products. The Gibbs free energy (ΔG) is

38   lower for incorporation with Na-bearing phases than with Fe-bearing phases, which is attributed

39   to the higher energetic stability of the iron sulfide minerals as a source phase for S than the

40   sodium sulfide phases. The thermodynamics of incorporation of reduced S are also evaluated by

41   using reaction equations involving dissolved disulfide and sulfide species ($H_nS_2^{(2-n)}{}_{(aq)}$ and $H_nS^{(2-}$

42    $^{n)}{}_{(aq)}$; n = 0, 1, and 2) as a source phase. The ΔG of S-incorporation increases for fluorapatite and

2

43   chlorapatite and decreases for hydroxylapatite as these species are protonated (i.e., as n changes

44   from 0 to 2). These thermodynamic results demonstrate that the presence of reduced S in apatite

45   is primarily controlled by the chemistry of magmatic and hydrothermal systems where apatite

46   forms (e.g., abundance of Fe; solution pH). Ultimately, our methodology developed for

47   evaluating the thermodynamics of S incorporation in apatite as a function of temperature, pH,

48   and composition is highly applicable to predicting the trace and volatile element incorporation in

49   minerals in a variety of geological systems. In addition to solid-solid and solid-liquid equilibria

50   treated here at different temperatures and pH, the methodology can be easily extended also to

51   different pressure conditions by just performing the quantum-mechanical calculations at elevated

52   pressures.

53   *Keywords:* Sulfur incorporation into apatite, oxybarometer, disulfide, bisulfide, sulfide,

54   fluorapatite, chlorapatite, hydroxylapatite, density functional theory (DFT) calculation.

55

56

3

Introduction

57

58   The behavior of sulfur (S) in earth systems is dependent on temperature (T), pressure (p),

59   oxygen (fO$_2$) and sulfur (fS$_2$) fugacity, and the composition (X) of the S-bearing fluid (i.e.,

60   hydrothermal or silicate melt (Carroll and Webster, 2018; Webster et al., 2011). Sulfur is a

61   polyvalent element that can co-exist in multiple oxidation states (e.g., S^{6+}, S^{4+}, S^0, S^{1-} and S^{2-})

62   and serves as an important ligand for the transportation and enrichment of metals (e.g., Cu, Fe,

63   Ni, Ag, and Au) and critical elements (e.g., REEs) in magmatic-hydrothermal and hydrothermal

64   systems (Piccoli and Candela, 2002; Simon and Ripley, 2011; Wan et al., 2021). In silicate melts,

65   sulfur is predominantly present as S^{6+} and/or S^{2-} (Baker and Moretti, 2011; Jugo, 2009; Jugo et

66   al., 2010). However, previous studies have proposed intermediate oxidation states of sulfur (e.g.,

67   S^{4+}, S^0, and S^{1-}) that are stable in silicate melts (Matjuschkin et al., 2016; Métrich et al., 2009).

68   The S content at sulfide saturation (SCSS) and S content at sulfate saturation (SCAS) in

69   silicate melts and hydrothermal fluids is controlled by *T-P-X* and the redox conditions of the

70   system (Baker and Moretti, 2011; Fiege et al., 2015; Jugo, 2009; Keppler, 1999; Kleinsasser et

71   al., 2022; Simon and Ripley, 2011; Zajacz et al., 2012). The S content in reduced silicate melts

72   (fO$_2$ below ~FMQ, where FMQ refers to the fayalite-magnetite-quartz fO$_2$ buffer) is typically on

73   the order of a few tens to a few hundred parts per million (ppm) of dissolved S as sulfide,

74   whereas oxidized (fO$_2$ above ~FMQ+2) and water-rich silicate melt may contain up to 1.5 wt% S

75   dissolved as sulfate (Jugo, 2009; Jugo et al., 2005). The preservation of primary magmatic

76   sulfate minerals (e.g., anhydrite) is rare in the volcanic rock record, owing to the dissolution of

77   anhydrite by meteoric water (Jakubowski et al., 2002; Luhr et al., 1984). For this reason, S-

4

78   bearing minerals, where sulfate replaces major oxyanions in phosphate and silicate minerals,

79   such as apatite and scapolite, are more common (Parat et al., 2011; Webster and Piccoli, 2015).

80   Since the S oxidation state is sensitive to the system fO_2, the abundance of different oxidation

81   states of S (i.e., $S^{6+}/\Sigma S$ where $\Sigma S = [S^{2-} + S^{1-} + S^{4+} + S^{6+}]$) in S-bearing minerals can serve as a

82   proxy for the redox evolution of magmatic and magmatic-hydrothermal systems (Konecke et al.,

83   2017, 2019) .

84   Konecke et al. (2017, 2019) demonstrated experimentally that sulfur oxidation states in

85   apatite, $Ca_{10}(PO_4)_6(F,OH,Cl)_2$, vary as a function of fO_2 in mafic melts. Specifically, the XANES

86   data reported by those authors reveal that S^{2-} is the dominant oxidation state of S in igneous

87   apatite equilibrated at FMQ while S^{6+} is predominant over S^{4+} and S^{2-} as fO_2 increases from

88   FMQ+1.2 to FMQ+3. The data reported in those studies are the first to quantitatively

89   demonstrate that apatite incorporates S oxidation states other than S^{6+} (in the form of sulfate),

90   which has long been reported incorrectly to be the only possible redox state of S in natural

91   apatite. Several studies have documented the presence of oxidation states of S other than, and in

92   addition to, S^{6+} in natural apatite. Brounce et al. (2019) document the presence of S^{2-} in lunar

93   apatite within samples 12039 and 10044, which are, respectively, a 3.2 ± 0.05 billion year old,

94   low-TiO_2 basalt and a ~3.71–3.73 billion year old, high-TiO_2 basalt. Sadove et al. (2019) report

95   the coexistence of multiple oxidation states of S (S^{6+}, S^{4+}, S^{1-} and S^{2-}) in terrestrial apatite from

96   the Phillips Mine magnetite-sulfide mineral deposit, New York, USA. Their work proposed that

97   apatite grains with structurally incorporated reduced S species with oxidation states S^{1-} and S^{2-}

98   crystallized initially from a reduced, S-bearing hydrothermal fluids, followed by secondary

99   alteration (metasomatism) that resulted in the structural incorporation of oxidized S (i.e., S^{6+} and

5

100   S^{4+}) in apatite. Tassara et al. (2020) document the presence of S^{2-} in apatite within basaltic tephra

101   erupted from the the Los Hornitos monogenetic cones in central-southern Chile, which are

102   among the most primitive materials reported in the Southern Andes (olivine Mg# ≤ 92.5, and Ni

103   ≤ 5000 ppm). Meng et al. (2021) document the presence of S^{2-} in apatite from calc-alkaline

104   plutonic rocks associated with the Haib porphyry Cu deposit in the Paleoproterozoic

105   Richtersveld Magmatic Arc (southern Namibia), an interpreted mature island-arc setting. Meng

106   et al. (2022) document the presence of S^{2-} in primary apatite from tonalite-trondhjemite-

107   granodiorite (TTG) igneous rocks temporally associated with the ~2.7 Ga St-Jude and Clifford

108   porphyry-type Cu ± Au deposits in the Neoarchean southern Abitibi subprovince. In combination

109   with the experimental results of Konecke et al. (2017, 2019), these data from natural terrestrial

110   and lunar samples demonstrate that the S6+/ΣS ratio of apatite records the redox evolution of the

111   melts and fluids from which it crystallized.

112   There is a dearth of data that constrain the substitution mechanisms for S species with

113   different oxidation states in apatite. The presence of S^{6+} in natural apatite has been attributed to

114   the substitution of SO_4^{2-} for PO_4^{3-} (Pan and Fleet, 2002; Parat et al., 2011; Streck and Dilles,

115   1998), whereas the presence of S^{2-} in apatite was only recently confirmed (e.g., Konecke et al.,

116   2017, 2019; Sadove et al., 2019). Kim et al. (2017) computationally investigated

117   thermodynamically plausible scenarios for the presence of S^{2-} in apatite that agree with the

118   experimental observations reported by Konecke et al. (2017, 2019); e.g., 2(F, Cl, OH)$^-$ ⇔ S^{2-} +

119   vacancy. The results from Kim et al. (2017) demonstrated that S^{2-} behaves chemically like Cl$^-$ in

120   the c-axis channel of apatite and, therefore, can substitute for the column anions F$^-$, OH$^-$ and/or

121   Cl$^-$. Those authors highlighted the need for future investigation of the substitution mechanisms

6

122   for HS$^-$ and other possible S species substitutions in apatite since they may occur in

123   hydrothermal fluids when H$_2$S is deprotonated. The demonstrated presence of structurally bound

124   S^{1-} and S^{2-} in natural apatite (Sadove et al., 2019) also highlights the need for a theoretical

125   understanding of the incorporation mechanisms of reduced S species in apatite.

126   In this study, we apply and evaluate quantum-mechanical calculations to elucidate the

127   energetics and geometry of reduced S species (oxidation state of –1 and –2) incorporated in the

128   apatite structure. One S(–I) species, disulfide (S$_2{}^{2-}$), and two S(–II) species, bisulfide (HS$^-$), and

129   sulfide (S^{2-}) are investigated as possible forms of reduced S in apatite. The following plausible

130   substitution mechanisms were investigated: 2(F, Cl, OH)$^-$ $\leftrightarrow$ S$_2{}^{2-}$ + vacancy ; (F, Cl, OH)$^-$ $\leftrightarrow$

131   HS$^-$; 2(F, Cl, OH)$^-$ $\leftrightarrow$ S^{2-} + vacancy. This computational approach permits the determination of:

132   [1] the energetic favorability of S incorporation into apatite depending on the occupancy of the

133   column anion and [2] the geometric and electrostatic constraints on the atomic site upon S

134   incorporation. The results demonstrate the potential role of S-in-apatite as a proxy to trace redox

135   conditions in magmatic and hydrothermal systems. This study builds on that of Kim et al. (2017),

136   which was based on the molecular energies at 0 K, by including computationally expensive

137   phonon analyses for the computation of enthalpy (including c_pT terms) and Gibbs free energy

138   contributions (including $-T\Delta S$ terms) for thermodynamics analyses. Both solids and aqueous

139   species were included as a source and sink, which is a significant advancement in applying

140   computational quantum-mechanical approaches to understanding the incorporation of redox-

141   sensitive elements in minerals.

7

METHODS

Computational parameters

Energy optimizations were performed using the quantum-mechanical code CASTEP (Segall et al., 2002). Computational constraints that successfully addressed sulfur species with different oxidation states in apatite were adopted from Kim et al. (2017). While optimizations were applied to configurations of mineral structures, the cell parameters and atomic positions were subject to modification to achieve minimum energies of the systems. The computational code is based on density functional theory (DFT). The Perdew-Wang generalized gradient scheme (GGA) was used along with ultrasoft pseudopotentials and parameterized by the Perdew–Burke–Ernzerhof (PBE) functional (Perdew et al., 1996). The energy cutoff for planewave expansion was 400.0 eV, and the Brillouin zone was sampled using a k-point separation of 0.05 $Å^{-1}$ according to the Monkhorst-Pack scheme (Monkhorst and Pack, 1976). The convergence tolerance for energy change was 2.0 $\times10^{-6}$ eV/atom. The energy optimization yields the total electronic energy of a system at 0 K, which is termed molecular energy (E_{mol}) in this study.

The phonon density of state (DOS) was calculated using CASTEP after energy optimizations using norm-conserving pseudopotentials and the same convergence tolerance mentioned above. The linear response methodology was used with a convergence criterion of 1.0×10^{-5} eV/ $Å^2$ for electronic eigenvalues and a k-point separation of 0.05 $Å^{-1}$. From the phonon DOS, the vibrational contributions to the Gibbs free energy (ΔG_{vib}) are evaluated for mineral species as the sum of the zero-point vibrational energy and the entropy correction (Baroni et al., 2001).
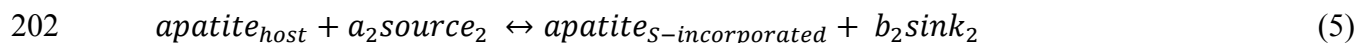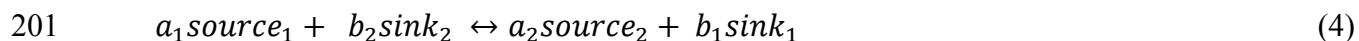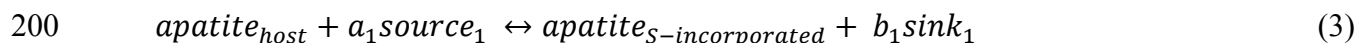
Incorporation energy calculations

163   Incorporation equations and energies of chemical species into a mineral are evaluated based

164   on periodic solid-state reactions. The background and principles of this approach are discussed in

165   detail in previous studies (Gebarski and Becker, 2020; Kim et al., 2017; Reich and Becker, 2006;

166   Shuller-Nickles et al., 2014; Shuller et al., 2010; Walker and Becker, 2015). Briefly, the general

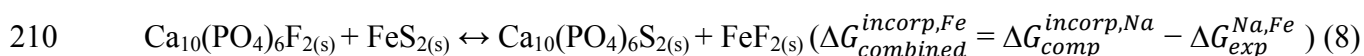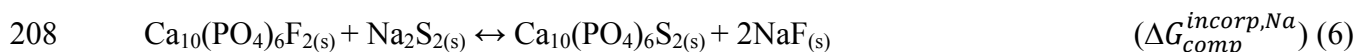167   equation and energy are explained as follows.

168    $$apatite_{host} + \sum_{i=1}^{n} a_i source_i \leftrightarrow apatite_{S-incorporated} + \sum_{i=1}^{m} b_i sink_i \qquad (1)$$

169    $$\Delta E_{rxn} = \sum E_{prod} - \sum E_{reac} \qquad (2)$$

170   A host apatite phase ($apatite_{host}$) with any of the three common anions on the column anion site

171   and sources for S ($source_i$) with different oxidation states are reactants, while S-incorporated

172   apatite ($apatite_{S-incorporated}$) and sinks for anions being released from the apatite host ($sink_i$) are

173   products. This approach allows for a consistent quantum-mechanical treatment, i.e., using the

174   same computational parameters throughout the equation, which is crucial to obtain reliable

175   energetic data. Once the molecular energies of all reactant and product phases are obtained from

176   energy optimization, the reaction energy (ΔE_{mol}) for an incorporation reaction is calculated using

177   Eq. 2. This incorporation reaction energy indicates the stability of the S-incorporated apatite

178   relative to the corresponding host apatite, as well as the source and sink phases. Furthermore,

179   enthalpy (ΔH) and Gibbs free energy (ΔG) of selected incorporation reactions are evaluated at

180   finite temperature (in this study, 25 ℃ and above) as the sum of total reaction energy (ΔE_{mol}),

181   zero-point energy (ΔE_{zp}), and the vibrational contributions (ΔH_{vib} and ΔG_{vib}) obtained from

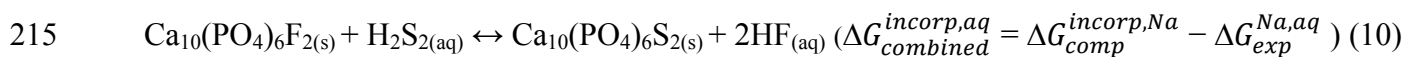182   energy optimizations and phonon analyses.

9

183   The thermodynamic data computed in this study were coupled with tabulated experimental

184   thermodynamic data (standard state and 25°C) to compare ΔG of incorporation reactions with

185   various source and sink phases. The first step of this procedure is to estimate computationally ΔG

186   of sulfur incorporation reactions into apatite (Tables 1 and 2) that involve Na-bearing source and

187   sink phases (denoted as $source_1$ and $sink_1$ in eq. 3). Among the source and sink phases examined

188   in this study, Na-bearing phases were chosen for this thermodynamic evaluation (i.e., energy

189   optimization followed by vibrational analysis) because they are computationally less demanding

190   than Fe-bearing phases or sinks and sources of dissolved ions. However, the latter two options of

191   sources and sinks (Fe-solids and aqueous reference species) were included by using

192   thermodynamic data from the literature. In a geological context, reaction equations involving Na-

193   bearing solid phases may represent model systems to simulate silicate melts where sodium is one

194   of the major elements and thus anions (like halide ions and reduced S species) may be present as

195   bonded with sodium ions (Na^+). Experimental thermodynamic data (Table S.1) were used to

196   calculate a balanced equation of a reaction (Eq. 4) that relates the Na-bearing phases with a

197   different kind of source and sink phase (denoted as $source_2$ and $sink_2$ in eq. 4). By combining

198   these two reaction equations (Eqs. 3 and 4), the reaction of S incorporation into apatite with

199   source and sink phases of interest (Eq. 5) and its ΔG are obtained.

200    $$apatite_{host} + a_1 source_1 \leftrightarrow apatite_{S-incorporated} + b_1 sink_1 \tag{3}$$

201    $$a_1 source_1 + b_2 sink_2 \leftrightarrow a_2 source_2 + b_1 sink_1 \tag{4}$$

202    $$apatite_{host} + a_2 source_2 \leftrightarrow apatite_{S-incorporated} + b_2 sink_2 \tag{5}$$

10

203   For instance, a reaction equation of disulfide incorporation into fluorapatite involving Na-bearing

204   source and sink phases is presented in Eq. 6. The ΔG of this reaction is evaluated from energy

205   optimization and phonon analysis. The ΔG of the reaction equation relating Na- and Fe-bearing

206   phases (Eq. 7) is obtained from tabulated thermodynamic data (Table S.1) and the ΔG of the

207   incorporation reaction involving Fe-bearing phases is estimated by combining Eq. 6 and 7.

208        $Ca_{10}(PO_4)_6F_{2(s)} + Na_2S_{2(s)} \leftrightarrow Ca_{10}(PO_4)_6S_{2(s)} + 2NaF_{(s)}$ $(\Delta G_{comp}^{incorp,Na})$ (6)

209        $Na_2S_{2(s)} + FeF_{2(s)} \leftrightarrow 2NaF_{(s)} + FeS_{2(s)}$ $(\Delta G_{exp}^{Na,Fe})$ (7)

210        $Ca_{10}(PO_4)_6F_{2(s)} + FeS_{2(s)} \leftrightarrow Ca_{10}(PO_4)_6S_{2(s)} + FeF_{2(s)}$ $(\Delta G_{combined}^{incorp,Fe} = \Delta G_{comp}^{incorp,Na} - \Delta G_{exp}^{Na,Fe})$ (8)

211   In the same manner, the ΔG of the incorporation reaction involving dissolved ionic species (Eq.

212   10) was estimated by using the equation relating Na-bearing phases and dissolved molecular

213   species (Eq. 9)

214        $Na_2S_{2(s)} + 2HF_{(aq)} \leftrightarrow 2NaF_{(s)} + H_2S_{2(aq)}$ $(\Delta G_{exp}^{Na,aq})$ (9)

215        $Ca_{10}(PO_4)_6F_{2(s)} + H_2S_{2(aq)} \leftrightarrow Ca_{10}(PO_4)_6S_{2(s)} + 2HF_{(aq)}$ $(\Delta G_{combined}^{incorp,aq} = \Delta G_{comp}^{incorp,Na} - \Delta G_{exp}^{Na,aq})$ (10)

216   In essence, this approach combines incorporation energies that can be computed purely at the

217   DFT level with the subsequent phonon calculations with experimental values for ΔG values of

218   formation of different source and sink phases to make the transition between different systems.

219   Applying this approach is particularly useful for evaluating the thermodynamics of incorporation

220   reactions   involving   reactant   and   product   phases   that   are   geologically   relevant,   but

11

221   computationally demanding (in this study, Fe-bearing minerals and ions dissolved in aqueous

222   solutions).

Structure models of apatite

224   The configuration models of the apatite endmembers are adopted from the natural apatite

225   structure, $[Ca_{10}(PO_4)_6(F,OH,Cl)_2]$ ($P6_3/m$; see Hughes et al., 1990; Hughes and Rakovan, 2015)

226   and are depicted in Figure 1. The apatite structure has two types of Ca sites, Ca1 and Ca2. The

227   Ca1 site is coordinated to nine O atoms, while the Ca2 site is coordinated to six O atoms and one

228   column anion (Fig. 1a and b). The three oxygen sites, O1, O2, and O3 in apatite, belong to the

229   constituent phosphate, forming the four corners of the tetrahedra whose center is P^{5+}. The Ca2

230   and O3 triangular planes are aligned along the c-axis, forming the channel (Fig. 1c), and the sites

231   within the c-axis channel (fractional coordinate = (0, 0, z)) are occupied by the main column

232   anions, F^-, OH^-, and Cl^- (Fig. 1a). The planes in which the Ca2 triangles occur (also called the

233   mirror planes) are located at z = 1/4 and 3/4 (Fig. 1a). The apatite endmembers are subdivided

234   into fluor-, hydroxyl- and chlorapatite based on a single occupant of the anion column, but often

235   occur in binary or ternary solid solution between/among the main column anions (Hughes et al.,

236   1990; Hughes and Rakovan, 2002). Thus, the c-axis channel has the potential to accommodate

237   foreign anions with different radii and/or charge. One well-known example is carbonate (CO_3^{2-})

238   substituting for OH^- in hydroxylapatite (Fleet and Liu, 2007) as it is common in bones and teeth

239   as it allows for greater flexibility to form a variety of morphologies.

240   Among the main column anions, fluorine is the smallest and located on the mirror planes at z

241   = 1/4 and 3/4 at the center of the Ca triangle (Fig. 1a). Hydroxide and chlorine do not fit in the

12

242   center of the Ca2 triangle and are thus displaced above or below the planes. There are multiple

243   positions of OH$^-$ and Cl$^-$ along the c-axis channel (Hughes and Rakovan, 2015). Since all atoms

244   in apatite must be given full atomic occupancy for quantum-mechanical modeling, the OH$^-$ and

245   Cl$^-$ positions below the planes at z = 1/4 and 3/4 were selected to complete the unit cell formula,

246   [$Ca_{10}(PO_4)_6(F,Cl,OH)_2$] (Fig. 1a). Thus, the structures of hydroxyl- and chlorapatite reduce the

247   symmetry to the $P6_3$ space group. Similar approaches to simulate hexagonal apatite without the

248   m symmetry have been successfully tested in previous computational studies (Corno et al., 2006;

249   Ulian et al., 2013). Using the structural and computational parameters above, a good agreement

250   in the unit cell parameters was found between calculated and experimental endmember apatites

251   reported by Hughes et al. (1989) (Table S.2). The resulting structures are then used to energy-

252   optimize the structure of the host and S-substituted apatite models.

253   It should be noted that in pure hydroxyl- and chlorapatite, the sense of ordering of hydroxide

254   or chloride in any individual column (e.g., above or below the mirror plane) causes the adjacent

255   column along the b axis to be ordered in the opposite direction (below or above the mirror plane)

256   (Hughes et al., 1989; Hughes and Rakovan, 2002). As a result, the symmetry of pure hydroxyl-

257   and chlorapatite degenerates to $P2_1/b$ (Elliott et al., 1973; Mackie et al., 1972). Most natural

258   hydroxyl and chlorapatite, however, are known to exist in the hexagonal space groups due to

259   impurities or vacancies in the anion columns (Hughes and Rakovan, 2002). In the apatite unit

260   cell and supercell models of this study, there is only one column along the c-axis and therefore,

261   the alternating ordering of hydroxide and chloride between adjacent columns is not included in

262   the energy-optimized structures. For this reason, the structural details of hydroxyl- and

13

263   chlorapatite reported from this study are more representative of natural hexagonal apatite

264   structures than pure monoclinic apatite structures.

Mechanisms of reduced S substitution

266   Although the major constituent column anions in apatite are F^-, OH^- and Cl^-, various

267   chemical substitutions can occur at the anion site in the c-axis channels of natural apatite. Pan

268   and Fleet (2002) compiled examples of substituent ions and molecules in the c-axis channel that

269   are monovalent, divalent, or neutral in charge and that can be monatomic, diatomic, or

270   polyatomic. Here, we focus on possible forms and substitution mechanisms of reduced S species

271   with oxidation states of –I and –II in apatite.

272   The first finding that S species can have an oxidation state of −1 in apatite was reported by

273   Sadove et al. (2019). Possible forms of S(−I) include monovalent and monoatomic S (S^-;

274   monoatomic sulfide) and divalent diatomic S (S_2^{2-}; disulfide) (Sadove et al., 2019). Since

275   monoatomic sulfide has the same charge as the major column anions, simple substitution for F^-,

276   OH^- and Cl^- is possible at the column anion site (Eq. 6). Since disulfide is divalent and the

277   column anion is monovalent in charge, the substitution of one disulfide for two column anions is

278   needed to maintain the total charge neutral (Eq. 7).

279        $(F,OH,Cl)^- \leftrightarrow S^-$ (6)

280        $2(F,OH,Cl)^- \leftrightarrow S_2^{2-} + vacancy$ (7)

281   The presence of oxidation state S(−II) in apatite has been demonstrated experimentally

282   (Konecke et al., 2017, 2019) and in natural samples (Sadove et al., 2019). As H_2S in a silicate

283   melt or hydrothermal fluid is deprotonated, S(−II) species may be partitioned into mineral phases

14

284   in the form of either bisulfide (HS^-) or sulfide (S^{2-}). Bisulfide can substitute for the column

285   anion via simple substitution (Eq. 8) due to the same charges whereas substitution of one sulfide

286   with two column anions (Eq. 9) is necessary for sulfide incorporation.

287        $(F,OH,Cl)^- \leftrightarrow HS^-$ (8)

288        $2(F,OH,Cl)^- \leftrightarrow S^{2-} + vacancy$ (9)

The structure model of S-substituted apatite

290   When the initial models (i.e., ones subjected to energy optimization) of sulfur-substituted

291   apatite were built, F^-, OH^- or Cl^- in the *c*-axis channel were replaced by reduced S species (S^-

292   and S_2^{2-} for S(–I); S^{2-} and HS^- for S(–II)) in unit cells or supercells of fluor-, hydroxyl- and

293   chlorapatite (based on Eqs. 6 to 9). During the process of energy optimization, the sulfide species

294   can be repositioned to any unoccupied position of the column and then relax to local minima in

295   the energy landscape. Therefore, in this study, it was examined whether there is an energetic or

296   geometric variation in the optimization result with different initial positions of S^{2-} in the anion

297   column. The position of F^-, Cl^-, and OH^- in the apatite anion column (i.e., (00z) obtained from

298   energy-optimizing the endmember apatite structures; Table S.2) was selected as the position of S

299   species in the initial models, unless stated otherwise. Where necessary, S species at those

300   positions are referred to as S(X)$_{ini}$ (where X = F, OH or Cl). Here, complete incorporation is

301   defined as S substitution wherein S is the only anion in the *c*-axis channel and partial

302   incorporation is when S replaces some fraction (< 1) of the column anions in the unit cell or

303   supercell of apatite.

15

304   For S(–I) in apatite, the calculated molecular energy of two monoatomic sulfide ions (S⁻) in

305   the c-axis channel is 90 kJ/mol higher compared to that of one disulfide (S_2^{2-}) (compare Fig. 2a

306   and c). This energy difference arises from the instability of monoatomic S^{-1} that has an unpaired

307   electron (i.e., a radical species). Therefore, further investigation for geometry and reaction

308   energy of S(–I) in apatite focuses on the incorporation of disulfide.

309   # RESULTS

310   ## Energy-optimized structures

311   This section focuses on the energy-optimized structures of disulfide, bisulfide, and sulfide,

312   replacing completely or partially the column anions in apatite. The optimization results indicate

313   structural responses of fluor-, chlor-, and hydroxylapatite to accommodating these species (Table

314   S.3) and energetic stability of reduced S species (indicated by its total energy, E_{mol}) as a function

315   of their position along the c-axis channel of apatite.

316   ### Disulfide (S_2^{2-})-incorporated apatite

317   Two possible models of complete incorporation of disulfide ($Ca_{10}(PO_4)_6(S_2)$) were built to

318   examine the stability of apatite phases having disulfide aligned parallel to the c-axis channel (Fig.

319   2). One model is that disulfide is positioned halfway between the Ca2 triangular planes (Fig. 2a).

320   In the other model, the center of disulfide is located on the mirror plane at $z = 1/4$ or $3/4$ (Fig. 2b).

321   From energy-optimization, the former model is 130 kJ/mol (in E_{mol}) more stable than the latter

322   one (Fig. 3a). In the energy-optimized structure of the former model, the two S atoms of

323   disulfide are located at (0, 0, 0.66) and (0, 0, 0.35), and the S-S distance in disulfide is 2.1 Å (Fig.

324   3a). This S-S bond length of disulfide in apatite is in good agreement with the molecular

16

325   geometry of hydrogen disulfide (H_2S_2) (Dixon et al., 1985). The cell parameters of disulfide-

326   incorporated apatite are listed in Table S.3. The unit cells of disulfide-incorporated apatite are 2

327   to 6 % longer in lattice parameters a and b and (< 2%) shorter in parameter c relative to their

328   respective host apatite, fluor-, chlor-, and hydroxylapatite.

329   Nine possible models of partial incorporation, in the form of $(Ca_{20}(PO_4)_{12}(S_2)(F,OH,Cl)_2)$

330   examine the atomic structure of disulfide interacting with neighboring column anions in the c-

331   axis channel (Fig. 4). The initial models (the ones prior to energy optimization) were built using

332   $1 \times 1 \times 2$ supercells of apatite in which the z value (with respect to the original unit cell) of the

333   anion in the c-axis channel ranges between 0 and 2. In the initial models, column anions, F^-, OH^-,

334   and Cl^-, are positioned on or below the mirror plane at $z = 7/4$ and $1/4$, while the centers of the

335   respective disulfide units are located at $z = 1/2$, $3/4$, and 1. The energy-optimized structures of

336   the nine possible models show that disulfide initially positioned at $z = 1/2$ and $3/4$ (Fig. 4b and c)

337   moves to $z \approx 1$ or remains near $z \approx 1/2$ while the major column anions move away. One reason

338   for this repositioning of the anions in the c-axis channel is repulsion between disulfide and the

339   column anions. In the optimized structure, disulfide is located halfway between the neighboring

340   column anions such that the repulsion between disulfide and the column anion is minimized. In

341   addition, it is energetically unfavorable for disulfide to be located on the mirror planes at $z = 3/4$

342   (Fig. 4c) because its stability is lower than when positioned between the mirror planes, as

343   demonstrated from the calculations on the complete incorporation of disulfide (Fig. 2).

344   Overall, the simulation results of complete and partial incorporation of disulfide predict that

345   disulfide is most energetically stable halfway between the mirror planes at $z = 1/4$ and $3/4$ in the

346   unit cell of apatite.

17

Bisulfide (HS⁻)-incorporated apatite

347

348   In the models of bisulfide replacing column anions entirely, $Ca_{10}(PO_4)_6(HS)_2$, bisulfide that is

349   initially positioned at the F site remains on the mirror planes at $z = 1/4$ and $3/4$ (equivalent to the

350   F site in apatite) while HS^- initially placed at the OH and Cl site is displaced from the mirror

351   plane by 0.04 in the z direction, which corresponds to the OH site in hydroxylapatite (Fig. 3b).

352   The calculated E_{mol} of complete incorporation of bisulfide is nearly the same (the difference ≈ 2

353   kJ/mol) for HS^- occupying the OH and F sites (Fig. 3b). The cell parameters of bisulfide-

354   incorporated apatite are listed in Table S.3. For lattice parameter a, the unit cells of bisulfide-

355   incorporated apatite are 1 to 5 % larger than the host apatite ones. The deviation of lattice

356   parameter c from the host apatite is less than 2 %.

357   Nine possible models of bisulfide partial incorporation, in the form of

358     $Ca_{10}(PO_4)_6(HS)(F,OH,Cl)$, examine bisulfide in apatite that interacts with neighboring column

359   anions (Fig. 5). In the initial models, bisulfide occupies the column anion sites on or below the

360   mirror plane at $z = 3/4$, while the neighboring F, OH, and Cl, are on or below the mirror plane at

361     $z = 1/4$. Like complete incorporation of bisulfide, the most favorable configurations of partially

362   incorporated bisulfide are close to the F and OH sites ($z = 0.68$ to 0.76) (Fig. 5). During energy

363   optimization, the z positions of neighboring F and OH change by less than 0.02 fractional unit

364   whereas the Cl position ($z = 0.07$ in chlorapatite; Fig. 5a) is shifted in the z direction toward the

365   mirror plane by 0.08 to 0.11 fractional units (Fig. 5b-d). The shifted positions of chlorine

366   indicate that the electrostatic interaction between the column anion and bisulfide is repulsive

367   such that the column anion moves away from bisulfide.

18

368   **Sulfide (S^{2-})-incorporated apatite**

369   Previous modeling work by Kim et al. (2017) investigated the complete and partial

370   incorporation of sulfide into the c-axis channel in apatite using the same computational

371   procedure as the present study. Here, a brief synopsis of their relevant results is provided.

372   In the complete incorporation model with the chemical formula of ($Ca_{10}(PO_4)_6S$),

373   incorporation of sulfide (S^{2-}) occurs at $z = 1/2$. This atomic position of sulfide in apatite is in

374   good agreement with experimental data for sulfoapatite (Henning et al., 2000). The calculated

375   E_{mol} of sulfide-incorporated apatite was found to be 130 kJ/mol lower for the unit cell of apatite

376   having sulfide at $z = 1/2$ than at $z = 3/4$ (equivalent to the F site in fluorapatite). This result

377   indicates that it is energetically unfavorable to accommodate sulfide on the F site in apatite.

378   The partial incorporation of sulfide into apatite was examined using nine possible

379   configuration models with stoichiometry ($Ca_{20}(PO_4)_{12}(S)(F,OH,Cl)_2$) (see Fig. 5 in Kim et al.

380   (2017)). The energy optimization results showed that sulfide in apatite is most energetically

381   stable when positioned at $z = 0.51$ to 0.61, which is close to the Cl site in natural apatite

382   (displacement by 0.18 in z value from the mirror planes). Like disulfide and bisulfide in apatite

383   (Fig. 4 and 5), it was found that neighboring F, Cl, and OH were shifted from their original

384   positions in the c-axis channel, due to repulsive interaction between the column anion and sulfide.

385   **Thermodynamics of reduced S incorporation into apatite**

386   The thermodynamics of disulfide, bisulfide, and sulfide incorporation into apatite were

387   evaluated for the reaction equations involving Na-bearing solids, Fe-bearing solids, and species

388   dissolved in aqueous solution as source and sink phases (Table 1 and 2). For the reactions
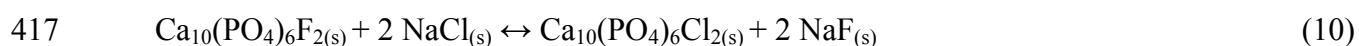
19

389 involving Na-bearing phases, we calculated all three thermodynamic entities, ΔE_{mol}, ΔH, and ΔG.

390 While ΔE_{mol} is the sum of the core-core, core-electron, and electron interaction in the system in

391 addition to the kinetic energy of the electrons (i.e., the "E" in the Schrödinger equation $H\Psi=E\Psi$

392 at 0 K), ΔH contains the zero-point vibrational energy (ZPE) and c_pT, and ΔG contains the ZPE,

393 c_pT, and the vibrational entropy term $-T\Delta S$. ΔG and ΔH values are derived using a quasi-

394 harmonic vibrational analysis at 25 ℃ and also at higher temperatures as described below. The

395 energetic properties (ΔE_{mol}, ΔH, and ΔG) of the equations involving Na-bearing phases are

396 computationally obtained, while the ΔG of equations involving Fe-bearing phases and dissolved

397 species are evaluated by combining the computed data with tabulated experimental

398 thermodynamic data (Table S.1) for "pure" (non-incorporated) source and sink phases (see

399 Methods section for details). The ΔG values of incorporation depend highly on selected source

400 and sink phases; this is not an artifact, as different source phases represent thermodynamically

401 stable minerals or solid compounds in different geochemical environments. These

402 thermodynamic data provide insights on physicochemical parameters controlling incorporation

403 of reduced S species into apatite in geological systems (see Discussion section).

404 **Disulfide incorporation into apatite**

405 The reaction equations and energies for complete and partial incorporation of disulfide into

406 apatite are presented in Table 1. There is a trend of Na-bearing phases that the enthalpy of

407 incorporation is higher than the molecular energy by 10 to 60 kJ/mol. Then, the entropy of the

408 reaction increases such that ΔG is less positive for fluor- and hydroxylapatite and more negative

409 for chlorapatite than ΔH. For the same Na-bearing, Fe-bearing, and aqueous source and sink

20

410   phases, the differences in ΔG between complete and partial incorporation reactions are less than

411   60 kJ/mol.

412   In the reactions involving Na-bearing phases, the ΔE_{mol}, ΔH, and ΔG of disulfide

413   incorporation is lowest for chlorapatite, followed by fluorapatite and hydroxylapatite. Complete

414   substitution (i.e., replacement) of Cl by disulfide is about 144 kJ/mol more favorable than

415   replacement of F and 189 kJ/mol more favorable than replacement of OH. These energy

416   differences are accounted for by the following reaction equations:

417    $Ca_{10}(PO_4)_6F_{2(s)} + 2\ NaCl_{(s)} \leftrightarrow Ca_{10}(PO_4)_6Cl_{2(s)} + 2\ NaF_{(s)}$ (10)

418    $Ca_{10}(PO_4)_6(OH)_{2(s)} + 2\ NaCl_{(s)} \leftrightarrow Ca_{10}(PO_4)_6Cl_{2(s)} + 2\ NaOH_{(s)}$ (11)

419   From the experimental thermodynamic data (Table S.1b; Drouet (2015)), the ΔG of Equations 10

420   and 11 are evaluated to be 90 kJ/mol ($\pm$ 97 kJ/mol) and 135 kJ/mol ($\pm$ 81 kJ/mol), which are

421   comparable with our DFT-calculated ΔG, 144 and 189 kJ/mol, respectively. The uncertainties of

422   these experimental ΔG values are equivalent to the standard deviation of the Gibbs free energy of

423   formation (ΔG_f^0) values of fluor-, chlor- and hydroxylapatite as compiled from previous studies

424   (Drouet (2015) and references therein).

425   In the reactions involving Fe-bearing phases, the ΔG of incorporation is lower for

426   chlorapatite and hydroxylapatite than for fluorapatite, which is in part because of the higher

427   stability of $Fe(OH)_{2(s)}$ as the sink phase than $FeF_{2(s)}$ and $FeCl_{2(s)}$. In general, the Gibbs free

428   energies of the reactions involving Na-bearing phases (-70 to 170 kJ/mol) are lower than those

429   involving Fe-bearing phases (190 to 350 kJ/mol). This outcome arises from the thermodynamic

430   stability of pyrite as a source phase for disulfide relative to $Na_2S_{2(s)}$.

21

431   For the treatment of hydrothermal source and sink phases, we considered dissolved

432   molecular species as source and sink phases (Table 1). $H_2S_{2(aq)}$, $HS_2^-{}_{(aq)}$, and $S_2^{2-}{}_{(aq)}$ (on the

433   reactant side) were used as source phases for disulfide and $HF_{(aq)}$, $F^-{}_{(aq)}$, $Cl^-{}_{(aq)}$, and $OH^-{}_{(aq)}$,

434    $H_2O_{(l)}$ (on the product side) were used as sink phases for the column anions. The protonation

435   states of disulfide and fluoride species change as a function of pH and their speciation diagrams

436   are presented in Figure S.1 (hydrochloric acid is always deprotonated). pK_{a1} and pK_{a2} of $H_2S_{2(aq)}$

437   are 5.0 and 9.7 and pK_{a1} of $HF_{(aq)}$ is 3.1. It follows that at pH below 5.0, $H_2S_{2(aq)}$ is the most

438   dominant disulfide species while both $HF_{(aq)}$ and $F^-{}_{(aq)}$ can exist in this pH range. At pH above

439   5.0, $HS_2^-{}_{(aq)}$ becomes dominant ($S_2^{2-}{}_{(aq)}$ at pH > 10), and F^- is the major fluoride species (Fig.

440   S.1). Considering these variations in speciation with pH, four possible reaction equations of

441   disulfide incorporation with $HF_{(aq)}$ and $F^-{}_{(aq)}$ as the sink phase, three reaction equations with Cl^-,

442   and three reaction equations with $OH^-{}_{(aq)}$ and $H_2O_{(l)}$ are balanced, and their Gibbs free energies

443   are evaluated (Table 1). Overall, the ΔG values for both complete and partial incorporation are

444   lower for chlor- and hydroxylapatite than for fluorapatite. Furthermore, by linearly combining

445   these reaction equations with protonated and deprotonated species, we evaluate the ΔG of

446   incorporation involving dissolved source and sink phases at equilibrium molar fractions that vary

447   as a function of pH (Fig. 6a and b). For both complete and partial incorporation, ΔG decreases

448   with pH for incorporation into fluor- and chlorapatite but increases with pH for hydroxylapatite.

449   Among the three host apatite phases, the ΔG of complete and partial incorporation is lowest for

450   hydroxylapatite at pH below 4 and for chlorapatite at pH above 5.

22

451 **Bisulfide incorporation into apatite**

452 The reaction equations and energies of complete and partial incorporation of bisulfide into

453 hydroxylapatite are presented in Table 2. The ΔG is 476 kJ/mol for complete incorporation and

454 227 kJ/mol for partial incorporation when $Na_2S_{(s)}$ and $Na_2O_{(s)}$ are source and sink. The ΔG of

455 reactions involving $NaSH_{(s)}$ and $NaOH_{(s)}$ is 193 kJ/mol for complete incorporation and 79 kJ/mol

456 for partial incorporation. The ΔG of incorporation with Fe-bearing phases is 208 and 93 kJ/mol

457 for complete and partial incorporation, respectively. The differences in Gibbs free energy

458 between the reactions involving different source and sink phases are attributed to the energetic

459 instability of $Na_2O_{(s)}$ as the sink phase relative to $NaOH_{(s)}$ and wüstite (FeO). For the

460 incorporation reactions involving molecular species dissolved in aqueous solutions, the ΔG of

461 incorporation with $H_2S_{(aq)}$ and $H_2O_{(l)}$ as the source and sink phases is 72 for complete

462 incorporation and 25 kJ/mol for partial incorporation. The ΔG of incorporation involving $HS^-_{(aq)}$

463 and $OH^-_{(aq)}$ is 171 and 74 kJ/mol for complete and partial incorporation, respectively. The

464 dependence of ΔG of incorporation on the protonation states of the source and sink phases

465 originates from the higher acidity of $H_2S_{(aq)}$ than $H_2O_{(l)}$ (pK_{a1} of H_2S is 5.0 and pK_a of H_2O is

466 15.7; Table S.1e).

467 **Sulfide incorporation into apatite**

468 The reaction equations and energies of complete and partial incorporation of sulfide into

469 fluor-, hydroxyl-, and chlorapatite are presented in Table 2. In the reactions involving Na-bearing

470 phases, the Gibbs free energy is lower for incorporation of sulfide into chlorapatite than that into

471 fluor- and hydroxylapatite. For incorporation into fluorapatite, the Gibbs free energy of partial

23

472   incorporation (209 kJ/mol) is about 90 kJ/mol higher than that of complete incorporation,

473   whereas the Gibbs free energy of partial incorporation into chlorapatite (-92 kJ/mol) is 45

474   kJ/mol lower than that of complete incorporation. This is in part because structural distortion

475   (indicated by a change in cell parameters; Table S.3) occurs to a lesser extent for accommodating

476   sulfide in chlorapatite than in fluorapatite. The Gibbs free energies of reaction involving Fe-

477   bearing phases are higher than those involving Na-bearing phases by 170 kJ/mol for

478   incorporation into fluorapatite, and by 210 kJ/mol for incorporation into chlorapatite. These

479   differences in Gibbs free energy come from the higher stability of troilite (FeS) as the source

480   phase (on the reactant side) compared to that of $Na_2S_{(s)}$.

481   In the reaction equations of incorporation involving dissolved molecular species (Table 2),

482   $H_2S_{(aq)}$, $HS^-_{(aq)}$, and $S^{2-}_{(aq)}$ (on the reactant side) are used as source phases for sulfide and $HF_{(aq)}$,

483   $F^-_{(aq)}$, $Cl^-_{(aq)}$, $H^+_{(aq)}$, $OH^-_{(aq)}$, and $H_2O_{(l)}$ (on the product side) as sink phases for the column

484   anions. At pH below 6.9, $H_2S_{(aq)}$ is the most dominant among the sulfide species, while both

485   $HF_{(aq)}$ and $F^-_{(aq)}$ can exist in this pH range (Fig. S.1). At pH above 6.9, $HS^-_{(aq)}$ and $S^{2-}_{(aq)}$ become

486   dominant and $F^-_{(aq)}$ is the major fluoride species. Like incorporation of disulfide, considering

487   these variations in speciation with pH, four possible reaction equations of disulfide incorporation

488   with $HF_{(aq)}$ and $F^-_{(aq)}$ as the sink phase and three reaction equations with $Cl^-_{(aq)}$ are balanced and

489   their Gibbs free energies are evaluated (Table 2). Overall, the ΔG of sulfide incorporation with

490   the same aqueous source phases is lower for chlorapatite than for fluorapatite by 150–190 kJ/mol

491   for complete incorporation and by 290–330 kJ/mol for partial incorporation (Table 2). From the

492   linear combination of these reaction equations with protonated and deprotonated species, we

493   calculate the ΔG of incorporation reactions in an aqueous environment with varying pH (Fig. 6c

494   and d). For both complete and partial incorporation, ΔG decreases with pH for incorporation into

495   fluor- and chlorapatite. This result indicates that incorporation of sulfide into apatite is

496   thermodynamically more favorable under alkaline conditions than neutral and acidic conditions.

Discussion

The stability of S species in the *c*-axis column channel

499   The modeling results of this study and Kim et al. (2017) demonstrate that the stability of

500   reduced S species (S_2^{2-}, HS^-, and S^{2-}) in apatite depends highly on the atomic sites that the

501   sulfide species occupy. In the energy-optimized configurations of S-incorporated apatite,

502   disulfide prefers to occupy the positions halfway between the mirror planes at $z = 1/4$ and $3/4$

503   (Fig. 3a and 4), whereas bisulfide is positioned slightly away (~ 0.04 in z value) from or on the

504   mirror planes (Fig. 3b and 5). Sulfide is most energetically stable when close to the Cl site in

505   apatite (Kim et al., 2017). In this section, some theoretical considerations are discussed to

506   explain how the energetic stability of the incorporated S species depends on the geometry and

507   the constituent elements (Ca and O atoms; Fig. 1c and d) of the *c*-axis channel.

508   The *c*-axis channel comprises O3 and Ca2 triangular planes perpendicular to the *c*-axis (Fig.

509   1c and d). Since the size and the electric charge (i.e., positively charged Ca vs. negatively

510   charged O planes) of the *c*-axis channel are changed with z, the position of a substituent ion that

511   occupies the *c*-axis channel can be determined by 1) electrostatic interaction of the substituent

512   anion with the Ca2 and O3 triangular planes and 2) the geometric constraint in the *c*-axis channel.

513   The electrostatic contribution is due to attractive and repulsive interactions between the Ca2/O3

25

514   plane and the substituent ion. Geometrically, substitution is likely to occur if the channel and the

515   substituent ion are similar in size.

516   The first step to quantify these constraints on a substituent ion in the c-axis channel is to

517   estimate the size of the c-axis channel of apatite as a function of z. We postulate that the channel

518   geometry is approximated by a series of circles along the c-axis tangent to the Ca2 and O3

519   triangular planes (Fig. 7a). The interatomic distances between calcium atoms on the Ca2 plane

520   and oxygen atoms on the O3 plane range from 4.0 to 4.4 and from 5.0 to 5.5 Å, respectively,

521   depending on the occupant of the column anion site (Table S.4). In the structure of fluor-, chlor-,

522   and hydroxylapatite, the estimated channel radii on the Ca2 planes range between 1.3 and 1.5 Å

523   and the O3 planes between 1.6 to 1.9 Å (Table S.4 and Fig. 7b).

524   Based on the estimated geometry of the c-axis channel, we examined whether the calculated

525   position of reduced S species, S_2^{2-}, HS^-, and S^{2-} in the c-axis channel is consistent with the

526   geometric and electrostatic constraints described above. Our calculation shows that disulfide in

527   the c-axis channel is the most energetically stable when its center is located halfway between the

528   mirror plane at $z = 1/4$ and 3/4 (Fig. 3a and 4). This geometry enables disulfide to maximize

529   attractive interaction with the positively charged Ca planes at $z = 1/4$ and 3/4 (electrostatic

530   contribution), while the two O3 planes at $z = 0.57$ and 0.43 have more spacious channels than the

531   Ca2 planes (Fig. 7b) to accommodate disulfide molecules (geometric contribution). For bisulfide

532   in apatite, the approximate size of HS^- (≈ 1.4 Å, the S-H distance of HS^-) falls within a range of

533   the channel radii of the Ca2 planes (1.3 and 1.5 Å; Fig. 7b). The difference in electronegativity

534   between sulfur and hydrogen generates the partial negative charge near sulfur and the partial

535   positive charge near hydrogen. The oxygen in the O3 planes attracts the hydrogen of HS^-

26

536   whereas the hydrogen repels the calcium in the Ca2 plane. Therefore, the calculated position of

537   the S atom of HS$^-$ being slightly away from the mirror plane by ~0.04 in z value (Fig. 3b) is

538   explained by considering the geometric and electrostatic constraints. In the energy-optimized

539   structures of sulfide-incorporated apatite reported by Kim et al. (2017), sulfide (S^{2-}) in apatite is

540   displaced away from the mirror planes by 1.0 to 1.6 Å, which correspond to the atomic sites near

541   to the O3 planes at $z = 0.57$ and 0.43 ($\approx$ the Cl site in chlorapatite). Since the ionic radius of

542   sulfide (1.84 Å; Shannon (1976)) exceeds the channel radius of the Ca2 planes, it is energetically

543   stable when it is accommodated in wider channels around the O3 planes (Fig. 7b). Overall, the

544   positions of reduced S species in apatite calculated from our modeling approaches are in good

545   agreement with the geometric and electrostatic constraints of the c-axis column anion channel.

546   These examples of reduced S species demonstrate that the geometric and electrostatic

547   considerations on the c-axis channel can be useful to predict the behavior of chemical species

548   incorporated in apatite.

Parameters controlling the thermodynamics of reduced S in apatite in geological systems

549

550

551   In the computational approach of this study, the thermodynamics of disulfide, bisulfide, and

552   sulfide incorporation are evaluated using different source and sink phases (Table 1 and 2). In

553   general, the calculated energy of incorporation is lower for the reactions involving Na-bearing

554   phases than those involving Fe-bearing phases (like pyrite and troilite on the reactant side).

555   These results arise from the higher stability of these iron sulfide minerals as the source phase for

556   S compared to sodium sulfide phases. In turn, it is inferred that when S-incorporated apatite

557   occurs in association with sulfide minerals, the presence of reduced S species in apatite are

27

558   primarily controlled by the chemistry of a system where apatite forms (e.g., Fe-abundant vs.

559   depleted). This inference is consistent with Sadove et al. (2019), who reported the presence of

560   inclusions of pyrrhotite and pyrite in natural S-incorporated apatite from the Phillip magnetite-

561   sulfide mineral deposit, New York. Their data demonstrated that reduced S species were

562   partitioned between iron sulfide and apatite as those phases crystallized from a reduced, S-

563   bearing hydrothermal fluid.

564   Our computed data also indicate that the speciation of dissolved S species would be

565   important in controlling the thermodynamics of incorporation reactions in aqueous media. For

566   reactions with fluor- and chlorapatite as the host phases, incorporation of disulfide and sulfide in

567   deprotonated forms like S_2^{2-} and S^{2-} is more thermodynamically favorable than incorporation in

568   protonated forms. In contrast, protonation of sulfide increases the thermodynamic favorability of

569   disulfide and bisulfide incorporation into hydroxylapatite. These computational results

570   demonstrate that the form of S species incorporated in apatite (e.g., sulfide vs. bisulfide) could be

571   determined by fluid pH where apatite forms through aqueous processes (like low-temperature

572   aqueous and hydrothermal systems).

573   Temperature is another crucial parameter in controlling the thermodynamics of S

574   incorporation in geological environments such as magmatic and hydrothermal systems. To

575   demonstrate the effect of temperature on the thermodynamics, the Gibbs free energy of complete

576   and partial incorporation of disulfide with Na-bearing and Fe-bearing phases as a function of

577   temperature is evaluated using temperature-dependent ΔG values of incorporation (Fig. 8). For

578   Na-bearing systems, the ΔG of disulfide incorporation increases with temperature for fluor- and

579   chlorapatite but decreases with increasing temperature for hydroxylapatite. For Fe-bearing

28

580   systems, the ΔG of disulfide incorporation into fluor- and hydroxylapatite decreases, and that into

581   chlorapatite increases as temperature increases. Our computed thermodynamic data suggest that

582   the thermodynamic favorability of S incorporation into apatite is likely to be temperature-

583   dependent in geological systems. At elevated temperatures, there may be thermodynamic

584   advantages when disulfide is incorporated into fluor- and chlorapatite in Fe-enriched

585   environments and into hydroxylapatite in Fe-depleted conditions.

586   Our methodology that combines DFT-computed thermodynamic data with experimental

587   thermodynamic data has been demonstrated to have the potential for evaluating the

588   thermodynamics of S incorporation in apatite in various geological systems. The thermodynamic

589   data obtained from this approach can be used to predict partitioning of reduced S species

590   between apatite and other S-bearing minerals (in this study, pyrite, and troilite) under varying

591   temperature, pH, and composition. Our new approach opens up the possibility of using DFT-

592   modeling to establish the thermodynamic basis to support experimental and field observations on

593   element incorporation in minerals and to understand the underlying mechanism and

594   thermodynamics in more detail. In addition, it can inspire experimentalists for further evaluation.

595   For example, the calculations presented here indicate a strong preference for chlorapatite to

596   incorporate different S species than the other two host apatites, which should be easily verifiable

597   by experiments. In general, the full quantum-mechanical derivation of the thermodynamics of an

598   incorporation reaction is time-consuming, especially the Gibbs free energy portion that requires

599   phonon analysis which can be an order of magnitude more computationally expensive than the

600   molecular energy E_{mol} only. However, once the Gibbs free energies of related source and sink

601   phases are available, in solid or aqueous form, the transition to such a different reference model

29

602   is a matter of minutes. This step can then be taken further relatively easily to geochemical

603   mixtures.

604   It would be important to examine sources of errors in both the experimental and the

605   computational portion of this approach. As stated in one example above, applying Gibbs free

606   energies of formation from different literature studies can result in uncertainties of at least tens of

607   kJ/mol, making a critical evaluation of thermodynamic data necessary. The error in the

608   calculations is of a different nature. One caveat of calculations is that complete error analysis is

609   often more expensive than the calculation itself if the entire space of potential errors is scanned,

610   them either being computational parameters (DFT functional, basis functions, k point density,

611   pseudopotentials, or higher-order effects for heavy elements such as spin-orbit coupling or

612   relativistic effects) or model setup (the most notable one, here, is the unit cell size). Fortunately,

613   some of these effects cancel out because they may be similar on both sides of a given equation,

614   especially if oxidation states do not change across the equation.

615   In this study, we have evaluated the incorporation thermodynamics as a function of

616   speciation, temperature, and for some examples of aqueous source/sink phases, pH. Another

617   variable that is rather straightforward to modify is pressure. However, the derivation of

618   thermodynamics becomes very demanding at high temperatures when simulating reactions in

619   melts or hydrothermal solutions. Some questions that one would have to address are: Are solid

620   reference phases still a viable approximation or do they break down or even lose their internal

621   structure (melt)? Is the quasi-harmonic phonon approximation still holding true for phonon

622   calculations? How are solubility products and pKa values defined in hydrothermal solutions of

623   high p, T?

30

Implications

624

625   This study addresses the structural incorporation of reduced S species with the S(−II) and

626   S(−I) oxidation states into apatite and the response of the apatite structure to these substituents.

627   Other than sulfide (S^{2-}) that can substitute for column anions in the c-axis channel (Henning et

628   al., 2000; Kim et al., 2017), bisulfide (HS^-) is another potential form of sulfur species with

629   oxidation state S(−II) in apatite via simple substitution of $HS^- \leftrightarrow (F, OH, Cl)^-$. Of the two

630   simplest S(−I) species, disulfide (S_2^{2-}) is the energetically more stable and plausible form in

631   apatite than monoatomic sulfide (S^-). In general, the energetic stability and crystallographic

632   characteristics of the S species in the c-axis channel of apatite vary depending on the S oxidation

633   state and chemical forms (S_2^{2-}, HS^-, and S^{2-}) and can be affected by (1) the neighboring column

634   anion (F^-, OH^- or Cl^-) and (2) geometric and electrostatic constraints by the Ca2 and O3 planes

635   along the c-axis.

636   The presence of volatile elements (especially, halogens, sulfur, and carbon) in apatite is

637   ubiquitous in igneous and hydrothermal environments (Webster and Piccoli, 2015). Although

638   historically, S^{6+} has been considered the most dominant oxidation state of sulfur in natural

639   apatite (c.f., Parat et al. (2011)), recent studies have demonstrated the strong dependence of the S

640   oxidation state in apatite as a function of oxygen fugacity (fO_2) and the formation of apatite

641   containing variable proportions of S^{6+}, S^{4+}, S^{1-} and S^{2-} as crystallized from magmatic and

642   hydrothermal fluids (Konecke et al., 2017, 2019; Sadove et al., 2019). In line with these previous

643   studies, the modeling of different S species in the apatite structure in this study implies that the

644   oxidation state of S in apatite has the potential to serve as a geochemical proxy to probe the fO_2

645   and fS_2 of magmatic and hydrothermal systems.

31

646

Acknowledgments

650

REFERENCES

651

652 Baker, D.R., and Moretti, R. (2011) Modeling the solubility of sulfur in magmas: a 50-year old
653   geochemical challenge. Reviews in Mineralogy and Geochemistry, 73(1), 167-213.

654 Baroni, S., De Gironcoli, S., Dal Corso, A., and Giannozzi, P. (2001) Phonons and related crystal
655   properties from density-functional perturbation theory. Reviews of Modern Physics, 73(2), 515.

656 Brounce, M., Boyce, J., McCubbin, F.M., Humphreys, J., Reppart, J., Stolper, E., and Eiler, J. (2019) The
657   oxidation state of sulfur in lunar apatite. American Mineralogist: Journal of Earth and Planetary
658   Materials, 104(2), 307-312.

659 Carroll, M.R., and Webster, J.D. (2018) Solubilities of sulfur, noble gases, nitrogen, chlorine, and fluorine
660   in magmas. Volatiles in magmas, 231-280.

661 Corno, M., Busco, C., Civalleri, B., and Ugliengo, P. (2006) Periodic ab initio study of structural and
662   vibrational features of hexagonal hydroxyapatite $Ca_{10}(PO_4)_6(OH)_2$. Physical Chemistry Chemical
663   Physics, 8(21), 2464-2472.

664 Dixon, D.A., Zeroka, D.J., Wendoloski, J.J., and Wasserman, Z.R. (1985) The molecular structure of
665   hydrogen disulfide (H_2S_2) and barriers to internal rotation. The Journal of Physical Chemistry,
666   89(25), 5334-5336.

667 Drouet, C. (2015) A comprehensive guide to experimental and predicted thermodynamic properties of
668   phosphate apatite minerals in view of applicative purposes. The Journal of Chemical
669   Thermodynamics, 81, 143-159.

670 Elliott, J.C., Mackie, P., and Young, R. (1973) Monoclinic hydroxyapatite. Science, 180(4090), 1055-
671   1057.

672 Fiege, A., Holtz, F., Behrens, H., Mandeville, C.W., Shimizu, N., Crede, L.S., and Göttlicher, J. (2015)
673   Experimental investigation of the S and S-isotope distribution between H_2O–S±Cl fluids and
674   basaltic melts during decompression. Chemical Geology, 393, 36-54.

675 Fleet, M.E., and Liu, X. (2007) Coupled substitution of type A and B carbonate in sodium-bearing apatite.
676   Biomaterials, 28(6), 916-926.

677 Gebarski, B.B., and Becker, U. (2020) Quantum-mechanical determination of the incorporation of
678   pentavalent plutonium into carbonate and sulfate minerals. Geochimica et Cosmochimica Acta,
679   269, 693-710.

680 Henning, P., Adolfsson, E., and Grins, J.J.Z.f.K.-C.M. (2000) The chalcogenide phosphate apatites
681     $Ca_{10}(PO_4)_6S$, $Sr_{10}(PO_4)_6S$, $Ba_{10}(PO_4)_6S$ and $Ca_{10}(PO_4)_6Se$. 215(4), 226-230.

682 Hughes, J.M., Cameron, M., and Crowley, K.D.J.A.M. (1989) Structural variations in natural F, OH, and
683   Cl apatites. 74(7-8), 870-876.

684 Hughes, J.M., Cameron, M., and Crowley, K.D. (1990) Crystal structures of natural ternary apatites; solid
685   solution in the $Ca_5(PO_4)_3X$ (X= F, OH, Cl) system. American Mineralogist, 75(3-4), 295-304.

686 Hughes, J.M., and Rakovan, J. (2002) The crystal structure of apatite, $Ca_5(PO_4)_3(F, OH, Cl)$. Reviews in
687   Mineralogy and Geochemistry, 48(1), 1-12.

688 Hughes, J.M., and Rakovan, J.F.J.E. (2015) Structurally robust, chemically diverse: apatite and apatite
689   supergroup minerals. 11(3), 165-170.

33

690   Jakubowski, R.T., Fournelle, J., Welch, S., Swope, R., and Camus, P. (2002) Evidence for magmatic
691   vapor deposition of anhydrite prior to the 1991 climactic eruption of Mount Pinatubo, Philippines.
692   American Mineralogist, 87(8-9), 1029-1045.

693   Jugo, P.J., Luth, R.W., and Richards, J.P. (2005) Experimental data on the speciation of sulfur as a
694   function of oxygen fugacity in basaltic melts. Geochimica et Cosmochimica Acta, 69(2), 497-503.

695   Jugo, P.J. (2009) Sulfur content at sulfide saturation in oxidized magmas. Geology, 37(5), 415-418.

696   Jugo, P.J., Wilke, M., and Botcharnikov, R.E. (2010) Sulfur K-edge XANES analysis of natural and
697   synthetic basaltic glasses: Implications for S speciation and S content as function of oxygen
698   fugacity. Geochimica et Cosmochimica Acta, 74(20), 5926-5938.

699   Keppler, H. (1999) Experimental evidence for the source of excess sulfur in explosive volcanic eruptions.
700   Science, 284(5420), 1652-1654.

701   Kim, Y., Konecke, B., Fiege, A., Simon, A., and Becker, U. (2017) An ab-initio study of the energetics
702   and geometry of sulfide, sulfite, and sulfate incorporation into apatite: The thermodynamic basis
703   for using this system as an oxybarometer. American Mineralogist: Journal of Earth and Planetary
704   Materials, 102(8), 1646-1656.

705   Kleinsasser, J., Simon, A.C., Konecke, B.A., Beckmann, P., and Holtz, F. (2022) Sulfide and sulfate
706   saturation of dacitic melts as a function of oxygen fugacity. Geochimica et Cosmochimica Acta,
707   In press.

708   Konecke, B.A., Fiege, A., Simon, A.C., Parat, F., and Stechern, A. (2017) Co-variability of S^{6+}, S^{4+}, and
709   S^{2-} in apatite as a function of oxidation state: Implications for a new oxybarometer. American
710   Mineralogist, 102(3), 548-557.

711   Konecke, B.A., Fiege, A., Simon, A.C., Linsler, S., and Holtz, F. (2019) An experimental calibration of a
712   sulfur-in-apatite oxybarometer for mafic systems. Geochimica et Cosmochimica Acta, 265, 242-
713   258.

714   Luhr, J.F., Carmichael, I.S., and Varekamp, J.C. (1984) The 1982 eruptions of El Chichón Volcano,
715   Chiapas, Mexico: mineralogy and petrology of the anhydritebearing pumices. Journal of
716   volcanology and geothermal research, 23(1-2), 69-108.

717   Mackie, P., Elliot, J., and Young, R. (1972) Monoclinic structure of synthetic Ca5 (PO4) 3Cl, chlorapatite.
718   Acta Crystallographica Section B: Structural Crystallography and Crystal Chemistry, 28(6),
719   1840-1848.

720   Matjuschkin, V., Blundy, J.D., and Brooker, R.A. (2016) The effect of pressure on sulphur speciation in
721   mid-to deep-crustal arc magmas and implications for the formation of porphyry copper deposits.
722   Contributions to Mineralogy and Petrology, 171(7), 1-25.

723   Meng, X., Kleinsasser, J.M., Richards, J.P., Tapster, S.R., Jugo, P.J., Simon, A.C., Kontak, D.J., Robb, L.,
724   Bybee, G.M., and Marsh, J.H. (2021) Oxidized sulfur-rich arc magmas formed porphyry Cu
725   deposits by 1.88 Ga. Nature communications, 12(1), 1-9.

726   Meng, X., Richards, J.P., Kontak, D.J., Simon, A.C., Kleinsasser, J.M., Marsh, J.H., Stern, R.A., and Jugo,
727   P.J. (2022) Variable modes of formation for tonalite-trondhjemite-granodiorite-diorite (TTG)-
728   related porphyry-type Cu±Au deposits in the Neoarchean southern Abitibi subprovince (Canada):
729   Evidence from petrochronology and oxybarometry. Journal of Petrology.

34

730 Métrich, N., Berry, A.J., O'Neill, H.S.C., and Susini, J. (2009) The oxidation state of sulfur in synthetic
731   and natural glasses determined by X-ray absorption spectroscopy. Geochimica et Cosmochimica
732   Acta, 73(8), 2382-2399.

733 Monkhorst, H.J., and Pack, J.D. (1976) Special points for Brillouin-zone integrations. Physical review B,
734   13(12), 5188.

735 Pan, Y., and Fleet, M.E. (2002) Compositions of the apatite-group minerals: substitution mechanisms and
736   controlling factors. Reviews in Mineralogy and Geochemistry, 48(1), 13-49.

737 Parat, F., Holtz, F., and Streck, M.J. (2011) Sulfur-bearing magmatic accessory minerals. Reviews in
738   Mineralogy and Geochemistry, 73(1), 285-314.

739 Perdew, J.P., Burke, K., and Ernzerhof, M. (1996) Generalized gradient approximation made simple.
740   Physical review letters, 77(18), 3865.

741 Piccoli, P.M., and Candela, P.A. (2002) Apatite in igneous systems. Reviews in Mineralogy and
742   Geochemistry, 48(1), 255-292.

743 Reich, M., and Becker, U. (2006) First-principles calculations of the thermodynamic mixing properties of
744   arsenic incorporation into pyrite and marcasite. Chemical Geology, 225(3-4), 278-290.

745 Sadove, G., Konecke, B.A., Fiege, A., and Simon, A.C. (2019) Structurally bound S^{2-}, S^{1-}, S^{4+}, S^{6+} in
746   terrestrial apatite: The redox evolution of hydrothermal fluids at the Phillips mine, New York,
747   USA. Ore Geology Reviews, 107, 1084-1096.

748 Segall, M., Lindan, P.J., Probert, M.a., Pickard, C.J., Hasnip, P.J., Clark, S., and Payne, M. (2002) First-
749   principles simulation: ideas, illustrations and the CASTEP code. Journal of Physics: Condensed
750   Matter, 14(11), 2717.

751 Shannon, R. (1976) Revised effective ionic radii and systematic studies of interatomic distances in halides
752   and chalcogenides. Acta crystallographica section A: crystal physics, 32(5), 751-767.

753 Shuller-Nickles, L.C., Bender, W.M., Walker, S.M., and Becker, U. (2014) Quantum-mechanical
754   methods for quantifying incorporation of contaminants in proximal minerals. Minerals, 4(3), 690-
755   715.

756 Shuller, L.C., Ewing, R.C., and Becker, U. (2010) Quantum-mechanical evaluation of Np-incorporation
757   into studtite. American Mineralogist, 95(8-9), 1151-1160.

758 Simon, A.C., and Ripley, E.M. (2011) The role of magmatic sulfur in the formation of ore deposits.
759   Reviews in Mineralogy and Geochemistry, 73(1), 513-578.

760 Streck, M.J., and Dilles, J.H. (1998) Sulfur evolution of oxidized arc magmas as recorded in apatite from
761   a porphyry copper batholith. Geology, 26(6), 523-526.

762 Tassara, S., Reich, M., Konecke, B.A., González-Jiménez, J.M., Simon, A.C., Morata, D., Barra, F.,
763   Fiege, A., Schilling, M.E., and Corgne, A. (2020) Unraveling the Effects of Melt–Mantle
764   Interactions on the Gold Fertility of Magmas. Frontiers in Earth Science, 8, 29.

765 Ulian, G., Valdrè, G., Corno, M., and Ugliengo, P. (2013) Periodic ab initio bulk investigation of
766   hydroxylapatite and type A carbonated apatite with both pseudopotential and all-electron basis
767   sets for calcium atoms. American Mineralogist, 98(2-3), 410-416.

768 Walker, S.M., and Becker, U. (2015) Uranyl (VI) and neptunyl (V) incorporation in carbonate and sulfate
769   minerals: Insight from first-principles. Geochimica et Cosmochimica Acta, 161, 19-35.

35

770   Wan, Y., Wang, X., Chou, I.-M., and Li, X. (2021) Role of sulfate in the transport and enrichment of REE
771   in hydrothermal systems. Earth and Planetary Science Letters, 569, 117068.

772   Webster, J.D., Goldoff, B., and Shimizu, N. (2011) C–O–H–S fluids and granitic magma: how S
773   partitions and modifies CO 2 concentrations of fluid-saturated felsic melt at 200 MPa.
774   Contributions to Mineralogy and Petrology, 162(4), 849-865.

775   Webster, J.D., and Piccoli, P.M. (2015) Magmatic apatite: A powerful, yet deceptive, mineral. Elements,
776   11(3), 177-182.

777   Zajacz, Z., Candela, P.A., Piccoli, P.M., Wälle, M., and Sanchez-Valle, C. (2012) Gold and copper in
778   volatile saturated mafic to intermediate magmas: Solubilities, partitioning, and implications for
779   ore deposit formation. Geochimica et Cosmochimica Acta, 91, 140-159.

780

781   **Table 1.** Reaction equations and energies of disulfide (S_2^{2-}) incorporation into apatite.

| complete incorporation	energy (kJ/mol)		
Na-bearing	ΔE_{mol}	ΔH	ΔG
$Ca_{10}(PO_4)_6F_{2(s)} + Na_2S_{2(s)} \leftrightarrow Ca_{10}(PO_4)_6S_{2(s)} + 2\ NaF_{(s)}$	108	155	128
$Ca_{10}(PO_4)_6Cl_{2(s)} + Na_2S_{2(s)} \leftrightarrow Ca_{10}(PO_4)_6S_{2(s)} + 2\ NaCl_{(s)}$	−22	−12	−16
$Ca_{10}(PO_4)_6OH_{2(s)} + Na_2S_{2(s)} \leftrightarrow Ca_{10}(PO_4)_6S_{2(s)} + 2\ NaOH_{(s)}$	157	175	173
Fe-bearing			ΔG
$Ca_{10}(PO_4)_6F_{2(s)} + FeS_{2(s)}\ (pyrite) \leftrightarrow Ca_{10}(PO_4)_6S_{2(s)} + FeF_{2(s)}$			342
$Ca_{10}(PO_4)_6Cl_{2(s)} + FeS_{2(s)}\ (pyrite) \leftrightarrow Ca_{10}(PO_4)_6S_{2(s)} + FeCl_{2(s)}$			239
$Ca_{10}(PO_4)_6OH_{2(s)} + FeS_{2(s)}\ (pyrite) \leftrightarrow Ca_{10}(PO_4)_6S_{2(s)} + FeOH_{2(s)}$			234
aqueous	ΔG (n =0)	ΔG (n =1)	ΔG (n=2)
$Ca_{10}(PO_4)_6F_{2(s)} + H_nS_2^{(n-2)}{}_{(aq)} \leftrightarrow Ca_{10}(PO_4)_6S_{2(s)} + n\ H^+ + 2\ F^-{}_{(aq)}$	199	244	273
$Ca_{10}(PO_4)_6F_{2(s)} + H_2S_{2(aq)} \leftrightarrow Ca_{10}(PO_4)_6S_{2(s)} + 2\ HF_{(aq)}$	–	–	237
$Ca_{10}(PO_4)_6Cl_{2(s)} + H_nS_2^{(n-2)}{}_{(aq)} \leftrightarrow Ca_{10}(PO_4)_6S_{2(s)} + n\ H^+ + 2\ Cl^-{}_{(aq)}$	32	77	105
$Ca_{10}(PO_4)_6OH_{2(s)} + H_nS_2^{(n-2)}{}_{(aq)} \leftrightarrow Ca_{10}(PO_4)_6S_{2(s)} + n\ H_2O_{(l)} + (2-n)\ OH^-{}_{(aq)}$	159	114	53
partial incorporation	energy (kJ/mol)		
Na-bearing	ΔE_{mol}	ΔH	ΔG
$2\ Ca_{10}(PO_4)_6F_{2(s)} + Na_2S_{2(s)} \leftrightarrow Ca_{20}(PO_4)_{12}F_2S_{2(s)} + 2\ NaF_{(s)}$	121	181	138
$2\ Ca_{10}(PO_4)_6Cl_2 + Na_2S_{2(s)} \leftrightarrow Ca_{20}(PO_4)_{12}Cl_2S_{2(s)} + 2\ NaCl_{(s)}$	−40	−56	−66
$2\ Ca_{10}(PO_4)_6OH_2 + Na_2S_{2(s)} \leftrightarrow Ca_{20}(PO_4)_{12}OH_2S_{2(s)} + 2\ NaOH_{(s)}$	164	175	164
Fe-bearing			ΔG
$2\ Ca_{10}(PO_4)_6F_2 + FeS_{2(s)}\ (pyrite) \leftrightarrow Ca_{20}(PO_4)_{12}F_2S_{2(s)} + FeF_{2(s)}$			352
$2\ Ca_{10}(PO_4)_6Cl_2 + FeS_{2(s)}\ (pyrite) \leftrightarrow Ca_{20}(PO_4)_{12}Cl_2S_{2(s)} + FeCl_{2(s)}$			188
$2\ Ca_{10}(PO_4)_6OH_2 + FeS_{2(s)}\ (pyrite) \leftrightarrow Ca_{20}(PO_4)_{12}OH_2S_{2(s)} + FeOH_{2(s)}$			225
aqueous	ΔG (n =0)	ΔG (n =1)	ΔG (n=2)
$2\ Ca_{10}(PO_4)_6F_{2(s)} + H_nS_2^{(n-2)}{}_{(aq)} \leftrightarrow Ca_{20}(PO_4)_{12}F_2S_{2(s)} + n\ H^+ + 2\ F^-{}_{(aq)}$	209	253	282
$2\ Ca_{10}(PO_4)_6F_{2(s)} + H_2S_{2(aq)} \leftrightarrow Ca_{20}(PO_4)_{12}F_2S_{2(s)} + 2\ HF_{(aq)}$	–	–	247
$2\ Ca_{10}(PO_4)_6Cl_{2(s)} + H_nS_2^{(n-2)}{}_{(aq)} \leftrightarrow Ca_{20}(PO_4)_{12}Cl_2S_{2(s)} + n\ H^+ + 2\ Cl^-(aq)$	−18	27	55
$2\ Ca_{10}(PO_4)_6OH_{2(s)} + H_nS_2^{(n-2)}{}_{(aq)} \leftrightarrow Ca_{20}(PO_4)_{12}OH_2S_{2(s)} + n\ H_2O_{(l)} + (2-n)\ OH^-{}_{(aq)}$	151	106	45

782

783

784

785

1

786 **Table 2.** Reaction equations and energies of sulfide (S^{2-}) and bisulfide (HS^-) incorporation into

787 apatite.

complete incorporation	energy (kJ/mol)		
Na-bearing	ΔE_{mol}	ΔH	ΔG
sulfide			
$Ca_{10}(PO_4)_6F_{2(s)} + Na_2S_{(s)} \leftrightarrow Ca_{10}(PO_4)_6S_{(s)} + 2\ NaF_{(s)}$	75	117	118
$Ca_{10}(PO_4)_6Cl_{2(s)} + Na_2S_{(s)} \leftrightarrow Ca_{10}(PO_4)_6S_{(s)} + 2\ NaCl_{(s)}$	−61	−70	−47
$Ca_{10}(PO_4)_6(OH)_{2(s)} + Na_2S_{(s)} \leftrightarrow Ca_{10}(PO_4)_6S_{(s)} + 2\ NaOH_{(s)}$	118	131	157
bisulfide			
$Ca_{10}(PO_4)_6(OH)_{2(s)} + 2\ Na_2S_{(s)} \leftrightarrow Ca_{10}(PO_4)_6(HS)_{2(s)} + 2\ Na_2O_{(s)}$	494	514	476
$Ca_{10}(PO_4)_6(OH)_{2(s)} + 2\ NaSH_{(s)} \leftrightarrow Ca_{10}(PO_4)_6(HS)_{2(s)} + 2\ NaOH_{(s)}$	171	186	193
Fe-bearing			ΔG
sulfide			
$Ca_{10}(PO_4)_6F_{2(s)} + FeS_{(s)}$ (troilite) $\leftrightarrow Ca_{10}(PO_4)_6S_{(s)} + FeF_{2(s)}$			285
$Ca_{10}(PO_4)_6Cl_{2(s)} + FeS_{(s)}$ (troilite) $\leftrightarrow Ca_{10}(PO_4)_6S_{(s)} + FeCl_{2(s)}$			160
bisulfide			
$Ca_{10}(PO_4)_6(OH)_{2(s)} + 2\ FeS_{(s)}$ (troilite) $\leftrightarrow Ca_{10}(PO_4)_6(HS)_{2(s)} + 2\ FeO_{(s)}$ (wüstite)			208
aqueous	ΔG (n =0)	ΔG (n =1)	ΔG (n=2)
sulfide			
$Ca_{10}(PO_4)_6F_{2(s)} + H_nS^{(n-2)}_{(aq)} \leftrightarrow Ca_{10}(PO_4)_6S_{(s)} + n\ H^+ + 2\ F^-_{(aq)}$	202	276	316
$Ca_{10}(PO_4)_6F_{2(s)} + H_2S_{(aq)} \leftrightarrow Ca_{10}(PO_4)_6S_{(s)} + 2\ HF_{(aq)}$			280
$Ca_{10}(PO_4)_6Cl_{2(s)} + H_nS^{(n-2)}_{(aq)} \leftrightarrow Ca_{10}(PO_4)_6S_{(s)} + n\ H^+ + 2\ Cl^-_{(aq)}$	14	88	127
bisulfide			
$Ca_{10}(PO_4)_6OH_{2(s)} + 2\ H_nS^{(n-2)}_{(aq)} \leftrightarrow Ca_{10}(PO_4)_6(HS)_{2(s)} + 2\ H_nO^{(n-2)}_{(l)}$	−	171	72
partial incorporation	energy (kJ/mol)		
Na-bearing	ΔE_{mol}	ΔH	ΔG
sulfide			
$2\ Ca_{10}(PO_4)_6F_{2(s)} + Na_2S_{(s)} \leftrightarrow Ca_{20}(PO_4)_{12}SF_{2(s)} + 2\ NaF_{(s)}$	185	247	209
$2\ Ca_{10}(PO_4)_6Cl_{2(s)} + Na_2S_{(s)} \leftrightarrow Ca_{20}(PO_4)_{12}SCl_{2(s)} + 2\ NaCl_{(s)}$	−69	−78	−92
$2\ Ca_{10}(PO_4)_6(OH)_{2(s)} + Na_2S_{(s)} \leftrightarrow Ca_{20}(PO_4)_{12}S(OH)_{2(s)} + 2\ NaOH_{(s)}$	244	253	260
bisulfide			
$Ca_{10}(PO_4)_6OH_{2(s)} + Na_2S_{(s)} \leftrightarrow Ca_{10}(PO_4)_6(HS)OH_{(s)} + Na_2O_{(s)}$	246	241	227
$Ca_{10}(PO_4)_6OH_{2(s)} + NaSH_{(s)} \leftrightarrow Ca_{10}(PO_4)_6(HS)OH_{(s)} + NaOH_{(s)}$	86	89	79
Fe-bearing			ΔG
sulfide			
$2\ Ca_{10}(PO_4)_6F_{2(s)} + FeS_{(s)}$ (troilite) $\leftrightarrow Ca_{20}(PO_4)_{12}SF_{2(s)} + FeF_{2(s)}$			376
$2\ Ca_{10}(PO_4)_6Cl_{2(s)} + FeS_{(s)}$ (troilite) $\leftrightarrow Ca_{20}(PO_4)_{12}SCl_{2(s)} + FeCl_{2(s)}$			114
bisulfide			
$Ca_{10}(PO_4)_6OH_{2(s)} + FeS_{(s)}$ (troilite) $\leftrightarrow Ca_{10}(PO_4)_6(HS)OH_{(s)} + FeO_{(s)}$ (wüstite)			93
aqueous	ΔG (n =0)	ΔG (n =1)	ΔG (n=2)
sulfide			
$2\ Ca_{10}(PO_4)_6F_{2(s)} + H_nS^{(n-2)}_{(aq)} \leftrightarrow Ca_{20}(PO_4)_{12}SF_{2(s)} + n\ H^+ + 2\ F^-_{(aq)}$	293	367	407
$2\ Ca_{10}(PO_4)_6F_{2(s)} + H_2S_{(aq)} \leftrightarrow Ca_{20}(PO_4)_{12}SF_{2(s)} + 2\ HF_{(aq)}$	−	−	371
$2\ Ca_{10}(PO_4)_6Cl_{2(s)} + H_nS^{(n-2)}_{(aq)} \leftrightarrow Ca_{20}(PO_4)_{12}SCl_{2(s)} + n\ H^+ + 2\ Cl^-_{(aq)}$	−32	42	82
bisulfide			
$Ca_{10}(PO_4)_6OH_{2(s)} + H_nS^{(n-2)}_{(aq)} \leftrightarrow Ca_{10}(PO_4)_6(SH)(OH)_{(s)} + H_nO^{(n-2)}_{(l)}$	−	74	25

2

788
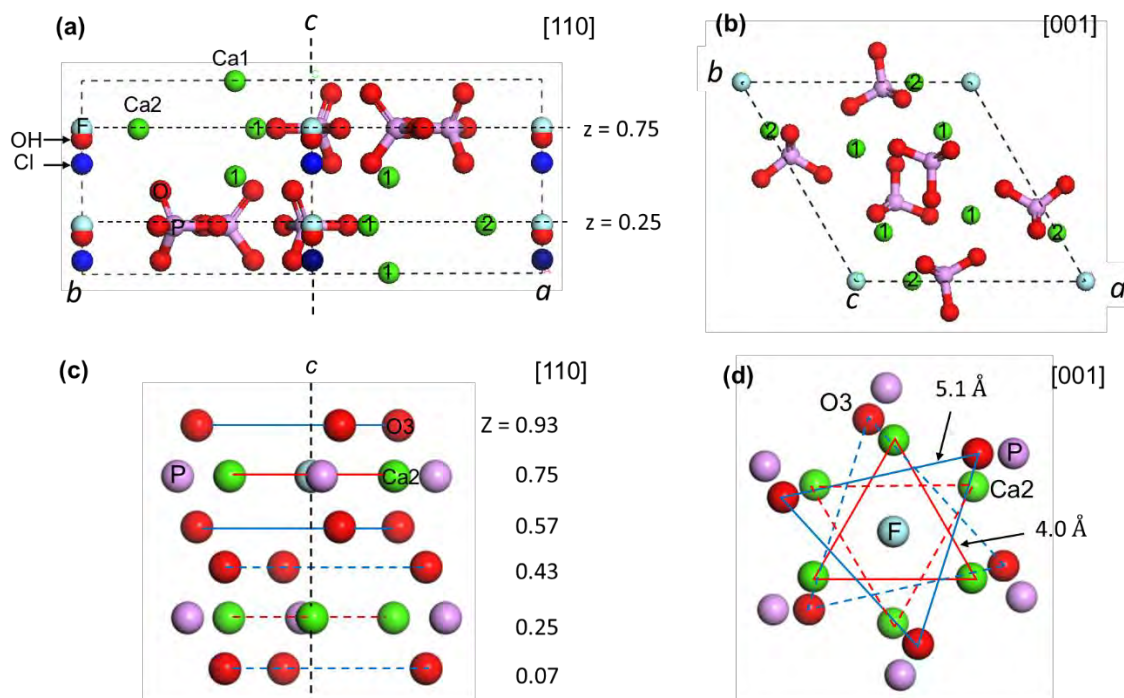
789

790   Figure 1. (a, b) The unit cell and (c, d) c-axis channel configurations of fluorapatite on view

791   of [110] and [001] direction. In (a), the relative positions (based on the z values; Table S.2) of

792   hydroxide and chloride are displayed in addition to fluorine. In (a, b), the Ca atoms labelled 1

793   and 2 represents two types of Ca sites, Ca1 and Ca2. In (d), the interatomic distances on each

794   Ca2 and O3 plane are measured and used to estimate the channel sizes (see Fig. 7 and text for
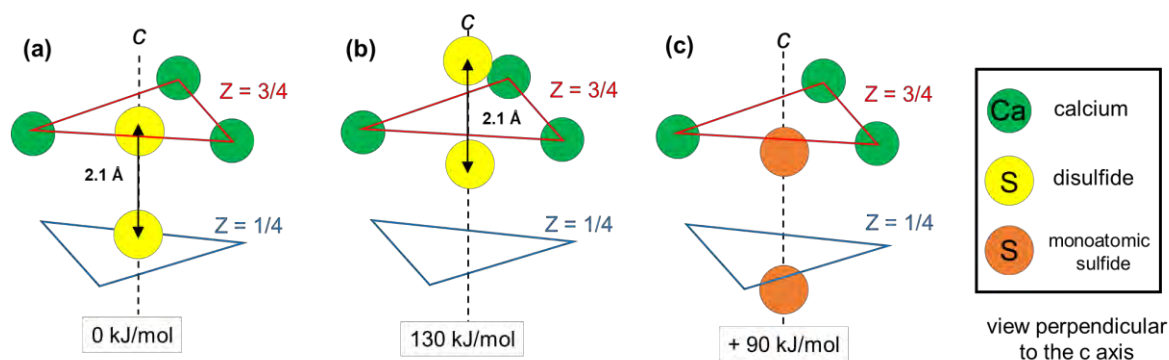
795   details).

796

797

798

799

3

800

801

Figure 2. Energy-optimized geometries of S(-I) species in apatite. The configurations of disulfide (a) with its center located at $z = 1/2$ (halfway between the mirror planes at $z = 1/4$ and 3/4) and (b) its center located at $z = 3/4$. The distance of the two S atoms is 2.1 Å as acquired from energy-optimization. (c) The configuration of monoatomic S(-I) atoms located below the mirror plane at $z = 1/4$ and 3/4. While all these configuration models represent the same composition of S-incorporated apatite, $(Ca_{10}(PO_4)_6S_2)$, the lowest molecular energy is found in the configuration described in (a). The energy values are with respect to this lowest-energy configuration.

811

812

813

4
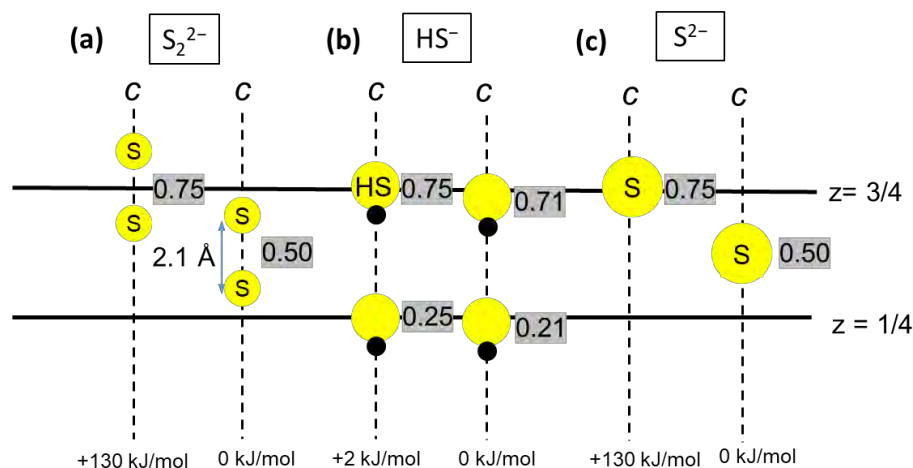
814

815 Figure 3. Energy-optimized structures of complete incorporation of (a) disulfide, (b) bisulfide,

816 and (c) sulfide into apatite. The two solid lines represent the mirror planes in apatite at $z = 1/4$

817 and 3/4. The z values (grey-highlighted) are specified to indicate the positions of the center of

818 disulfide in (a) and the positions of S atoms belonging to bisulfide and sulfide in (b, c). The

819 energy values are with respect to the lowest energy calculated for respective species in apatite.

820

821

5
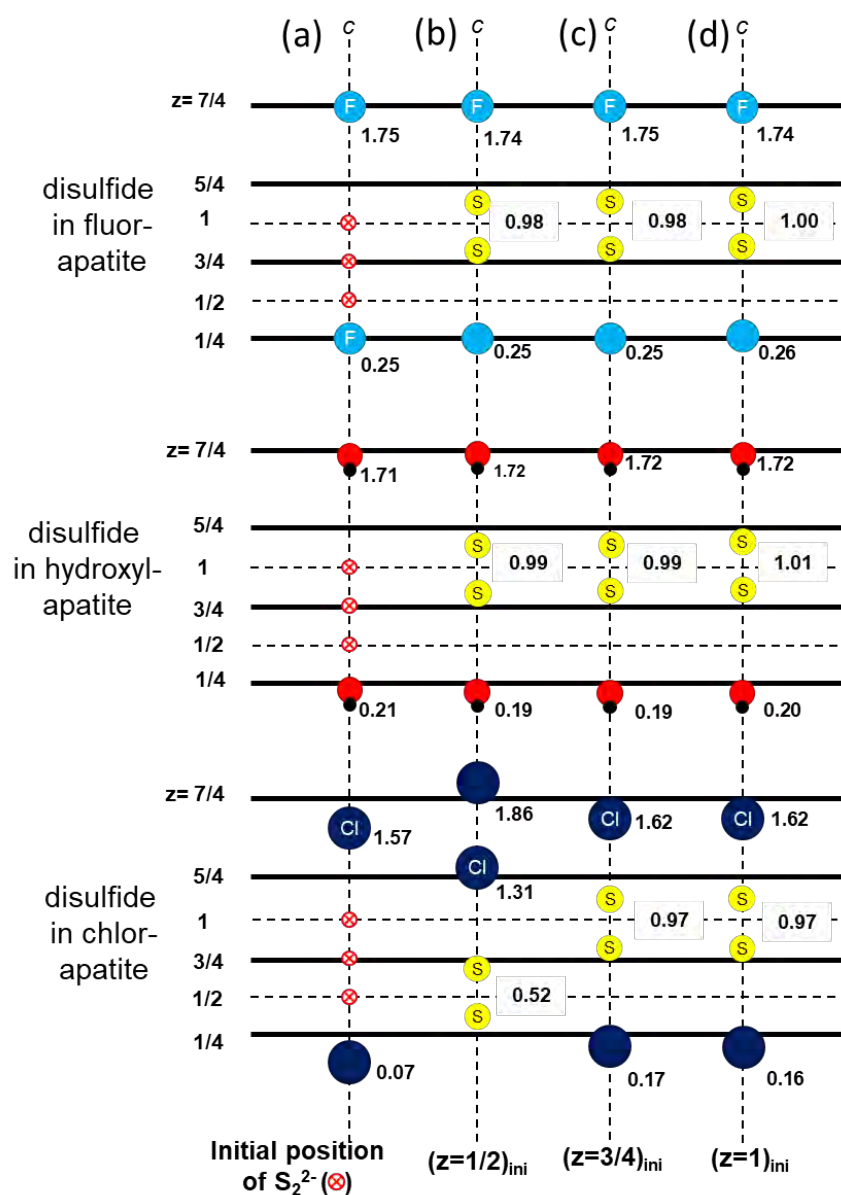
822

823   Figure 4. (a) Initial and (b to d) energy-optimized configurations (i.e., ones before and after

824   the process of energy optimization) for partial incorporation of disulfide in the c-axis column

825   anion channel in the form of $(Ca_{20}(PO_4)_{12}(S_2)(F,OH,Cl)_2)$. The z value (with respect to the unit

826   cell) of the anions in the c-axis channel ranges between 0 and 2. In the initial configurations, the

827   center of disulfide was positioned (b) at $z = 1/2$, (c) $z = 3/4$, and (d) $z = 1$.
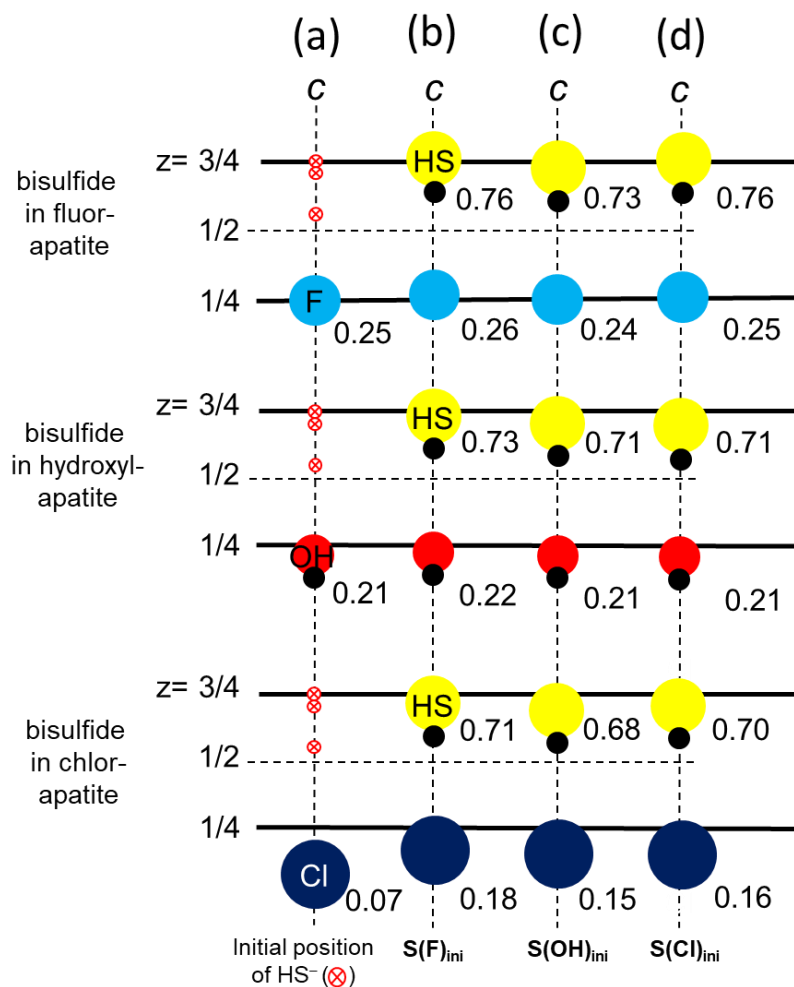
828

829   Figure 5. (a) Initial and (b to d) energy-optimized configurations for partial incorporation of

830   bisulfide in the c-axis channel of apatite in the form of $(Ca_{10}(PO_4)_6(HS)(F,OH,Cl))$. In the initial

831   configurations, bisulfide was positioned (b) at the fluorine, (c) hydroxide, and (d) chlorine sites

832   in the c-axis channel (denoted by $S(F,OH,Cl)_{ini}$).

833

834

835

7

(a) Complete incorporation of disulfide

$\gamma 1.\ Ca_{10}(PO_4)_6F_{2(s)} + n_1H_2S_{2(aq)} + n_2HS^-_{2(aq)} + n_3S^{2-}_{2\ (aq)}$
$\leftrightarrow Ca_{10}(PO_4)_6S_{2(s)} + (2n_1 + n_2 - 2k_1)H^+ + 2k_1HF + 2k_2F^-$

$\gamma 2.\ Ca_{10}(PO_4)_6(OH)_{2(s)} + n_1H_2S_{2(aq)} + n_2HS^-_{2(aq)} + n_3S^{2-}_{2\ (aq)}$
$\leftrightarrow Ca_{10}(PO_4)_6S_{2(s)} + (2n_1 + n_2)H_2O + (n_2 + 2n_3)OH^-$

$\gamma 3.\ Ca_{10}(PO_4)_6Cl_{2(s)} + n_1H_2S_{2(aq)} + n_2HS^-_{2(aq)} + n_3S^{2-}_{2\ (aq)}$
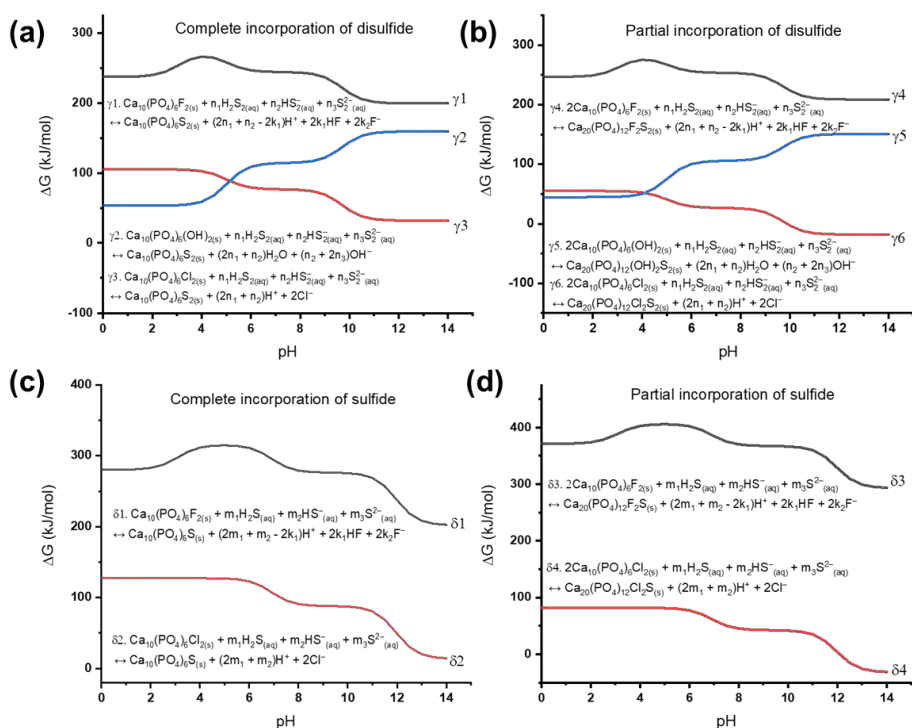$\leftrightarrow Ca_{10}(PO_4)_6S_{2(s)} + (2n_1 + n_2)H^+ + 2Cl^-$

(b) Partial incorporation of disulfide

$\gamma 4.\ 2Ca_{10}(PO_4)_6F_{2(s)} + n_1H_2S_{2(aq)} + n_2HS^-_{2(aq)} + n_3S^{2-}_{2\ (aq)}$
$\leftrightarrow Ca_{20}(PO_4)_{12}F_2S_{2(s)} + (2n_1 + n_2 - 2k_1)H^+ + 2k_1HF + 2k_2F^-$

$\gamma 5.\ 2Ca_{10}(PO_4)_6(OH)_{2(s)} + n_1H_2S_{2(aq)} + n_2HS^-_{2(aq)} + n_3S^{2-}_{2\ (aq)}$
$\leftrightarrow Ca_{20}(PO_4)_{12}(OH)_2S_{2(s)} + (2n_1 + n_2)H_2O + (n_2 + 2n_3)OH^-$

$\gamma 6.\ 2Ca_{10}(PO_4)_6Cl_{2(s)} + n_1H_2S_{2(aq)} + n_2HS^-_{2(aq)} + n_3S^{2-}_{2\ (aq)}$
$\leftrightarrow Ca_{20}(PO_4)_{12}Cl_2S_{2(s)} + (2n_1 + n_2)H^+ + 2Cl^-$

(c) Complete incorporation of sulfide

$\delta 1.\ Ca_{10}(PO_4)_6F_{2(s)} + m_1H_2S_{(aq)} + m_2HS^-_{(aq)} + m_3S^{2-}_{(aq)}$
$\leftrightarrow Ca_{10}(PO_4)_6S_{(s)} + (2m_1 + m_2 - 2k_1)H^+ + 2k_1HF + 2k_2F^-$

$\delta 2.\ Ca_{10}(PO_4)_6Cl_{2(s)} + m_1H_2S_{(aq)} + m_2HS^-_{(aq)} + m_3S^{2-}_{(aq)}$
$\leftrightarrow Ca_{10}(PO_4)_6S_{(s)} + (2m_1 + m_2)H^+ + 2Cl^-$

(d) Partial incorporation of sulfide

$\delta 3.\ 2Ca_{10}(PO_4)_6F_{2(s)} + m_1H_2S_{(aq)} + m_2HS^-_{(aq)} + m_3S^{2-}_{(aq)}$
$\leftrightarrow Ca_{20}(PO_4)_{12}S_{(s)} + (2m_1 + m_2 - 2k_1)H^+ + 2k_1HF + 2k_2F^-$

$\delta 4.\ 2Ca_{10}(PO_4)_6Cl_{2(s)} + m_1H_2S_{(aq)} + m_2HS^-_{(aq)} + m_3S^{2-}_{(aq)}$
$\leftrightarrow Ca_{20}(PO_4)_{12}Cl_2S_{(s)} + (2m_1 + m_2)H^+ + 2Cl^-$

836

837   Figure 6. Gibbs free energy (ΔG) is calculated as a function of pH, assuming thermodynamic

838   equilibrium at 25 °C, for (a, b) complete and partial incorporation of disulfide and (c, d) complete

839   and partial incorporation of sulfide into apatite using source and sink phases dissolved in

840   aqueous solution. The fractions of dissolved disulfide species, H_2S_2, HS_2^-, and S_2^{2-} (n_1, n_2, and n_3,

841   respectively, where $n_1 + n_2 + n_3 = 1$), sulfide species, H_2S, HS^-, and S^{2-} (m_1, m_2, and m_3,

842   respectively, where $m_1 + m_2 + m_3 = 1$), and F species, HF and F^- (k_1 and k_2, respectively, where

843    $k_1 + k_2 = 1$) vary as a function of pH as presented in Fig. S.1. These pH dependences of dissolved

844   S and F species are considered to balance the reaction equations.
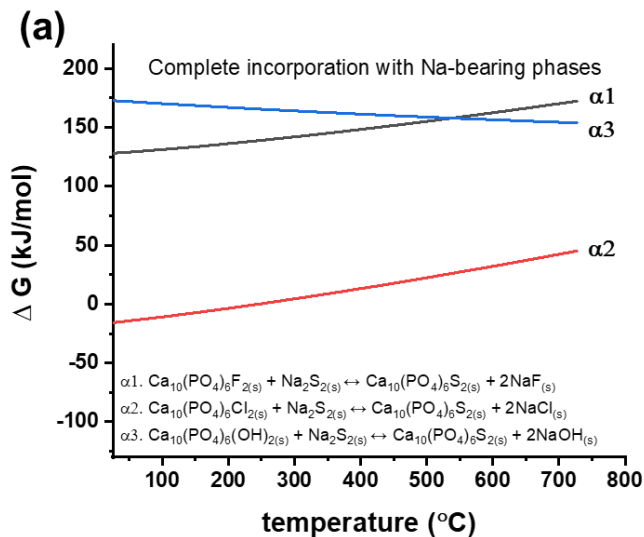
845

8
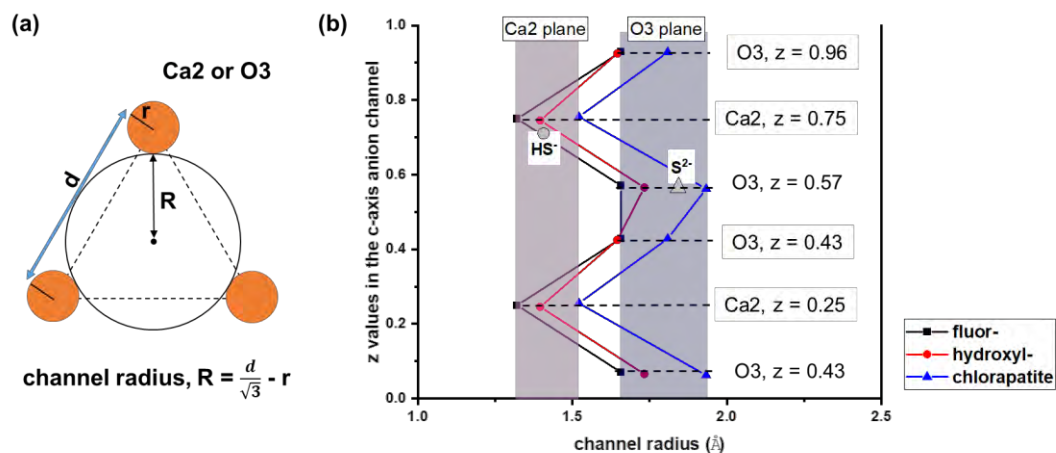
846

847   Figure 7. (a) The scheme to estimate the radius of the c-axis channel on the Ca2 and O3

848   planes in the apatite unit cell and (b) the variation in the radius of the c-axis anion channel of

849   fluor-, hydroxyl- and chlorapatite across the c-axis. In (b), the ionic radii of the substituent ions

850   (HS$^-$ and S^{2-}) and their energy-optimized positions in the c-axis channel are plotted with the grey
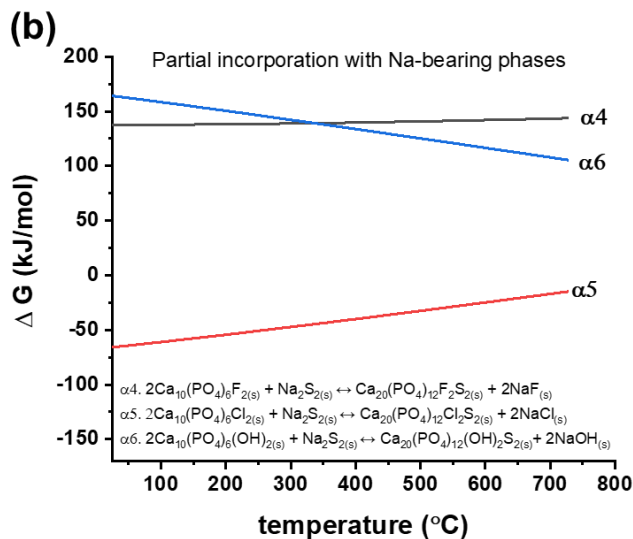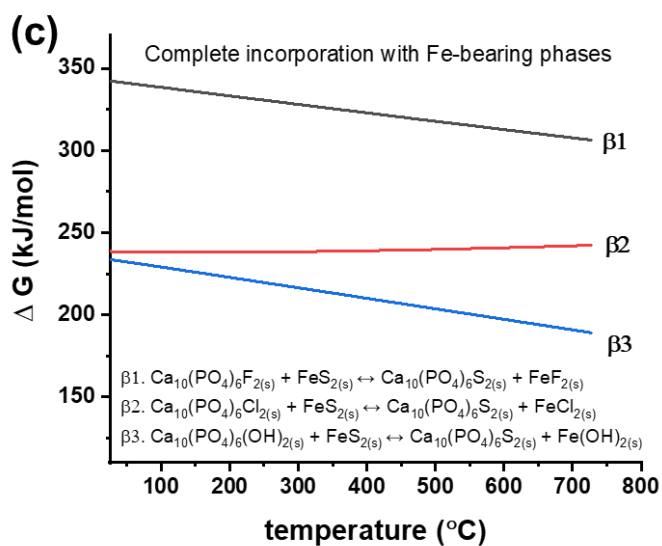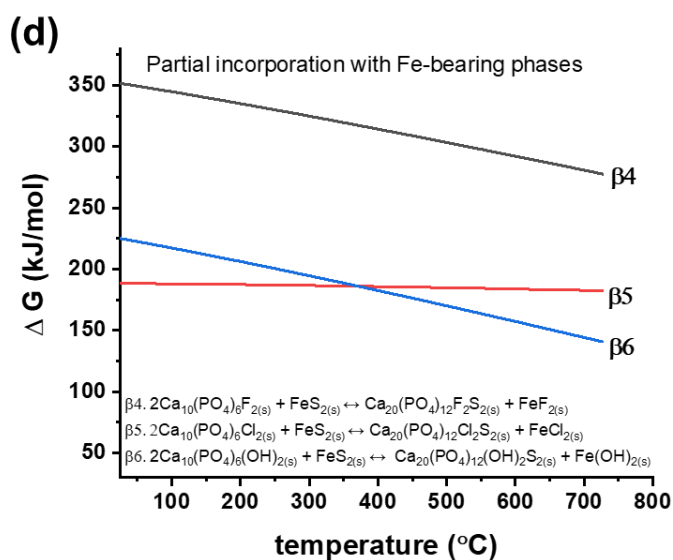
851   symbols.

852

853

854

9

(a)

855

(b)

856

857

858

859

10

(c)

Complete incorporation with Fe-bearing phases

$\beta1$. $Ca_{10}(PO_4)_6F_{2(s)} + FeS_{2(s)} \leftrightarrow Ca_{10}(PO_4)_6S_{2(s)} + FeF_{2(s)}$
$\beta2$. $Ca_{10}(PO_4)_6Cl_{2(s)} + FeS_{2(s)} \leftrightarrow Ca_{10}(PO_4)_6S_{2(s)} + FeCl_{2(s)}$
$\beta3$. $Ca_{10}(PO_4)_6(OH)_{2(s)} + FeS_{2(s)} \leftrightarrow Ca_{10}(PO_4)_6S_{2(s)} + Fe(OH)_{2(s)}$

860

(d)

Partial incorporation with Fe-bearing phases

$\beta4$. $2Ca_{10}(PO_4)_6F_{2(s)} + FeS_{2(s)} \leftrightarrow Ca_{20}(PO_4)_{12}F_2S_{2(s)} + FeF_{2(s)}$
$\beta5$. $2Ca_{10}(PO_4)_6Cl_{2(s)} + FeS_{2(s)} \leftrightarrow Ca_{20}(PO_4)_{12}Cl_2S_{2(s)} + FeCl_{2(s)}$
$\beta6$. $2Ca_{10}(PO_4)_6(OH)_{2(s)} + FeS_{2(s)} \leftrightarrow Ca_{20}(PO_4)_{12}(OH)_2S_{2(s)} + Fe(OH)_{2(s)}$

861

862   Figure 8. Gibbs free energy (ΔG) as a function of temperature for complete and partial

863   incorporation of disulfide with (a, b) Na-bearing and (c, d) Fe-bearing source and sink phases.

864

11